A cortico-subcortical loop for motor control via the pontine reticular formation

Emília Bősz[1, 2]*, Viktor M. Plattner[1, 3]*, László Biró[1]*, Kata Kóta[1, 2], Marco A. Diana[4] and László Acsády*[1]

Affiliations:

[1] Laboratory of Thalamus Research, Institute of Experimental Medicine; Budapest, Hungary

[2] János Szentágothai Doctoral School of Neurosciences, Semmelweis University, Budapest, Hungary

[3] Sainsbury Wellcome Ctr., London, United Kingdom

[4] Université Paris Cité, CNRS, Saint-Pères Paris Institute for the Neurosciences, F-75006 Paris, France

*Corresponding author: acsady@koki.hu

Laboratory of Thalamus Research, Institute of Experimental Medicine; Budapest, Szigony u. 43. 1083. Hungary

* These authors contributed equally to this work

Summary

Movement and locomotion are controlled by large neuronal circuits like the cortex-basal ganglia (BG)-thalamus loop. Inhibitory output of the BG loop can directly control movement via specialized connections with the brainstem. Whether other parallel loops with similar logic exist is presently unclear. Here we demonstrate that glycine transporter 2-positive (GlyT2+) cells of the pontine reticular formation (PRF) receive cortical inputs and in turn innervate the thalamus. Thalamus-projecting GlyT2+ cells innervate subcortical regions distinct from BG targets. Cortical cells co-innervate PRF/GlyT2+ cells and thalamus as in the BG loops. Cortex exerts strong excitatory control on PRF/GlyT2+ cells and these neurons powerfully inhibit their thalamic targets. Activation of thalamus projecting PRF/GlyT2+ cells leads to contralateral turning. These results demonstrate that the PRF is part of a cortico-subcortical loop that regulates motor activity parallel to the BG circuits. The cortico-PRF-thalamus loop can synergistically control turning with the BG loops via distinct descending pathways.

Keywords

Motor system, basal ganglia, brainstem, rotation, turning, thalamus, motor cortex, cingulate cortex, pons, locomotion, parafascicular thalamus, intralaminar thalamus

Introduction

Voluntary movements are controlled via diverse cortical and subcortical centers[1,2]. Among these, the basal ganglia (BG) are one of the most intensively studied and are thought to be responsible for the planning, execution, and learning of complex motor sequences[2–5]. Two key features characterize the BG circuits. First, cortex, BG, and thalamus are engaged in the formation of complex loops [6–8]; second, the output of these loops is communicated as a strong inhibitory signal to brainstem locomotor centers via the BG output nuclei [9,10].

The cortex-BG-thalamus loop can be regarded as a multiple-nested loop[11–13] since the cortical signals return to the cortex via both the direct, thalamo-cortical projections and via an indirect loop that passes through the BG and the thalamus [6–8]. Since the entire system is strongly topographical the indirect BG signals and the direct cortico-thalamic pathway are integrated in the same thalamic territory[6,8,14]. This pattern of connectivity is especially useful to generate multiple embedded rhythms, the hallmark of cortical and brainstem activity governing locomotion[1]. Individual cortical neurons can provide axon collaterals to both the direct thalamo-cortical pathway[15–17] and the indirect cortex-BG loop ensuring that an identical cortical message is transferred via these two nested pathways.

How the cortex-BG-thalamus loop communicates with the brainstem locomotor centers has been poorly investigated until recently. By now it appears that the BG innervates multiple brainstem locomotor centers and can have a strong impact on their activity[9]. A recent study[10] has demonstrated a specific role of the BG in regulating turning behavior via the pontine reticular formation (PRF, its rostral part also referred to as nucleus pontis oralis, PnO). PRF has already been implicated earlier in motor

67 control[18,19]. Cregg et al.,[10] showed that the substantia nigra pars reticulata (SNR), a
68 major output nucleus of the BG, can effectively inhibit in the excitatory vesicular
69 glutamate transporter 2 (vGLUT2)-containing neurons in the PRF. These
70 PRF/vGLUT2+ neurons, in turn, innervate the contralateral gigantocellular nucleus
71 (Gi) in the lower brainstem. Gi cells can mediate ipsiversive turning and motor arrest
72 via their direct reticulo-spinal connections [20,21]. The new study shows that decreased
73 inhibitory SNR output results in increased PRF/vGLUT2+ output which consequently
74 elevates contralateral Gi activity leading to a contralateral turning, relative to the side
75 of SNR-PRF interaction. Increased BG output has the opposite effect[10]. Modulating
76 the PRF/vGlut2+- Gi pathway restores turning ability after striatal damage, implying
77 that impairment in this pathway could contribute to the disabling turning deficits
78 associated with Parkinson's disease[10].These data demonstrate how the output of the
79 cortex-thalamus-BG loop can have direct behavioral consequences via modulating the
80 activity of the brainstem motor centers.

81 Curiously, the BG output avoided the other major cell type of the PRF, the equally
82 numerous inhibitory, glycine transporter 2-expressing cells (PRF/GlyT2+ cells)[10,22]. At
83 the same time, however, Gi neurons, ipsilateral to the turning, receive a strong
84 inhibition[10], the sources of which are unknown. PRF/GlyT2+ neurons have dual
85 GABAergic/glycinergic phenotype and can innervate the same thalamic regions (the
86 intralaminar/parafascicular nuclei, IL/Pf) as the BG-thalamic pathway[23]. IL/Pf have
87 already been also implicated in movement coordination, turning and orienting
88 behavior[24–26]. The thalamic projecting PRF/GlyT2+ cells establish large, highly
89 effective multisynaptic inhibitory terminals, very similar to those of the BG terminals in
90 the thalamus[23,27]. PRF is known to receive input from higher-order motor cortical
91 areas[28,29] and photoactivation of thalamus-projecting PRF/GlyT2+ cells results in

92 motor arrest[23]. These data indicate that, even though PRF/GlyT2+ cells are not
93 innervated directly by the BG output, they may participate in an independent cortico-
94 thalamic loop and can contribute to motor control.

95 Based on these data, in this study, we tested whether thalamic projecting
96 PRF/GlyT2+ neurons can represent a brainstem movement control system involved in
97 a nested loop organization with the cortex and thalamus that can contribute to turning
98 behavior. Our data demonstrate that thalamus-projecting PRF/GlyT2+ cells receive
99 strong cortical excitatory inputs, via cortical L5 neurons. L5 neurons, in addition to
100 innervating the PRF, also arborize in the IL/Pf, the target of PRF/GlyT2+cells. We also
101 show that thalamic projecting PRF/GlyT2+ cells can evoke pronounced inhibitory
102 action on their thalamic targets and affect turning behavior synergistically with the
103 PRF/vGLUT2+ cells via a selective ipsilateral projection to Gi.

104 Results

105 M2/cingulate cortical neurons innervate PRF/GlyT2+ neurons

106 In order to visualize cortical inputs to PRF/GlyT2+ neurons, we used anterograde
107 virus-mediated tracing in RBP4-Cre//GlyT2-eGFP double transgenic mice. RBP4 is
108 known to be expressed in deep L5 pyramidal cells the project to subcortical targets[30].
109 We injected AAV5-DIO-ChR2-mCherry virus into the secondary motor/cingulate
110 (M2/Cg) cortical area since these regions is known to contain the highest
111 concentration of PRF projecting cells[23] (Figure 1A-C). GlyT2+ cells were detected by
112 the eGFP expression[22]. Anterogradely labeled M2/Cg fibers formed a profuse axon
113 arbor within the entire rostral PRF (Figure 1D-F). The distribution of cortical afferents
114 displayed significant overlap with that of the PRF/GlyT2+ neurons (Figure 1D-F) but
115 was not homogeneous within the PRF. A density map of cortical afferents showed a

116 dorsomedial to ventrolateral decrease in fiber density within the PRF/GlyT2+ zone
117 (Figure 1G, S1A-C). This gradient was present at all coronal levels examined on
118 averaged maximum intensity projection of the fiber density maps in 3 animals (Figures
119 1H1-3, S1A-C). Caudal injections into the M2/Cg cortex (n=3) resulted in weaker PRF
120 innervation (Figure 1I). The quantitative analysis of intensity levels showed that the
121 whole PRF was innervated by M2/Cg (Figure 1J). The posterior M2/Cg afferents
122 displayed low-intensity levels (2-4) compared to the anterior M2/Cg innervation where
123 we observed higher fiber density (intensity levels 1-7, Figure 1K).

124 Next, we visualized anterior M2/Cg fibers and PRF/GlyT2+ neurons using high-
125 power confocal imaging and high-power light microscopy using DAB/Ni (black) and
126 DAB (brown) chromogens. With both methods, cortical afferents were in close
127 proximity to PRF/GlyT2+ elements (Figure 1L). We found putative synaptic contacts
128 on the dendrites and occasionally on the somata of GlyT2+ neurons (Figure 1M, N).
129 In one case the spine of a PRF/GlyT2+ neuron, filled using the juxtacellular labeling
130 method (see below), was found to be contacted by an M2/Cg cortical terminal (Figure
131 1O).

132 In order to identify the synaptic contacts formed by M2/Cg terminals in the PRF,
133 we analyzed the ultrastructure of the M2/Cg synapses at the electron microscopic level
134 (Figure 2A-D). M2/Cg terminals were small to medium-sized (mean=0.47 μm^2
135 SD=0.31, Figure 2B-D, S1D), contained 1-3 mitochondria, and established
136 asymmetrical synapses with 1-2 active zones mainly with dendrites (range: 0.197-
137 1.437 μm, mean=0.62 μm, SD=0.31, Figure 2B-D). The postsynaptic elements have
138 variable diameters. Using double immunocytochemistry we identified synaptic
139 contacts between virus-labeled cortical afferents and PRF/GlyT2+ neurons in 10

140 cases (Figure 2D1-4). In 9 cases the postsynaptic structure was mid-caliber dendrite
141 in 1 case it was a PRF/GlyT2+ spine. These data show that the anterior M2/Cg
142 provides a dense innervation to the PRF, which contains GlyT2+ neurons and forms
143 conventional synaptic contacts mainly with the dendrites of GlyT2+ neurons in the
144 PRF.

145 ## Synaptic properties of the cortical inputs in PRF/GlyT2+ neurons

146 Next, we investigated the physiology of synapses formed by the cortico-PRF
147 terminals in GlyT2+ cells. In vitro, PRF slice preparations were made from RBP4-
148 Cre//GlyT2-eGFP animals that received identical AAV5-DIO-ChR2-mCherry M2/Cg
149 injections as in the case of the anterograde tracing experiments. Optogenetic
150 activation with brief flashes (2-3 ms) of blue light evoked synaptic. At a recording
151 potential of -60 mV, these triggered rapidly rising and decaying inward synaptic
152 currents with an averaged amplitude amounting to 48.6 ± 20.2 pA; (Figure 2E, bottom
153 panel). The amplitude of these responses was not modified by bath application of the
154 GABAergic/glycinergic synaptic blockers SR95531 (2 μM) and strychnine (10 μM),
155 thus demonstrating their excitatory nature. When recorded at a holding potential of
156 +50 mV (see methods), the EPSCs showed clearly slower decaying kinetics than at -
157 60 mV consistently with the appearance of an NMDA receptor-mediated component
158 at the depolarized potential (Figure 2E, top panel, blue traces). Bath co-application of
159 NBQX (10 μM) and DL-APV (50 μM), led to almost complete inhibition of the synaptic
160 responses to 5.6 ± 1.4 % of the control at -60 mV, and to 10.1 ± 3.0 % at +50 mV
161 (Figure 2E, top red traces), thus demonstrating the glutamatergic nature of the cortico-
162 PRF/GlyT2+ inputs. The amplitude of the NMDA component, as measured at +50 mV,
163 amounted to 68.7 ± 15.3 % of the AMPA component at -60 mV (Figure 2E). Moreover,
164 the AMPA rectification index (measured as the ratio between the AMPA component

165 amplitudes at -60 mV and at +50 mV) amounted to 1.9 ± 0.3 (n = 17; Figure 2E bottom),
166 not distant from the theoretical value of 1.75 for a linear I-V curve (see Otsu et al.,
167 2018). This strongly suggests that the AMPA receptors present at these synapses are
168 calcium-impermeable in PRF/GlyT2+ neurons.

169 In control pharmacological conditions, we examined the dynamic behavior of the
170 cortico-PRF glutamatergic responses with trains of 10 optogenetic stimulations at
171 different frequencies (1 Hz, 5 Hz, 10 Hz and 20 Hz). Along the stimulation trains the
172 synaptic responses in the PRF/GlyT2+ cells did not show a significantly depressing
173 behavior, the amplitude of the responses to the 10th stimulation being significantly
174 smaller than the one to the first light pulse only at 5 Hz (see top traces in Figure 2F).
175 With respect to the first optogenetic stimulation, the amplitudes of the responses to
176 the 10th light pulse were indeed 89.1 ± 11.5 %, 87.3 ± 8.2 %, 102.7 ± 5.7 %, 90.5 ±
177 14.0 % at 1 Hz, 5 Hz, 10 Hz, and 20 Hz, respectively (see bottom graph in Figure 2F).
178 These data demonstrate that the cortical inputs to the PRF/GlyT2+ neurons identified
179 morphologically exert a pronounced, conventional, purely glutamatergic synaptic
180 action with little short-term depression.

181 ## The impact of cortical activation on PRF/GlyT2+ neuronal activity

182 In order to assess the impact of cortical inputs on the spiking activity of
183 PRF/GlyT2+ neurons *in vivo,* we recorded the evoked responses of the PRF cells in
184 ketamine-xylazine anesthetized animals (n=10 animals, Figure 3). In 7 cases we
185 injected the AAV5-DIO-ChR2-mCherry virus into M2/Cg in the RBP4-Cre//GlyT2-
186 eGFP double transgenic mice and photostimulated the L5 neurons (Figure 3A-B). In
187 3 cases we applied bipolar electrical stimulation of the cortex in GlyT2/GFP transgenic
188 mice (5 ms pulse width, 1-2 mA). In both stimulating conditions, we used trains of 1,
189 10, and 20 Hz stimulations (n=50 stimulus in 5 trains, Figure S2). To unequivocally

190 identify and localize PRF/GlyT2+ neurons we used the juxtacellular recording and
191 labeling methods[31]. Nine out of 10 neurons were recovered post hoc within the PRF
192 and their GlyT2+ identity was determined by double fluorescent imaging (Figures 3C,
193 and S2A).

194 Cortical stimulation at 1 Hz generated reliable spike responses with short latency
195 peaks, in all PRF/GlyT2+ cells (Figure 3D-E) using both stimulation methods.
196 Increasing the stimulation frequency to 10 and 20 Hz resulted in similar high-fidelity,
197 fast responses (Figure 3D-E). We found no significant difference between stimulation
198 frequencies in response probability and latency (Figure 3F) indicating reliable signal
199 transmission even at high presynaptic activity. To assess the alteration of firing output
200 of the PRF/GlyT2+ cells within the stimulation train at various input frequencies, we
201 calculated the normalized evoked AP within a 50 ms time window after every stimulus
202 (Figure S2B). The data demonstrated that the spiking activity of individual PRF/GlyT2+
203 cells did not depress within the stimulus train irrespective of the stimulation
204 frequencies (Figure S2B). These in vivo data confirm the in vitro physiological data
205 and show that frontal cortical cells can evoke fast, reliable spike responses in
206 PRF/GlyT2+ cells even at high presynaptic stimulation frequencies.

207 ## Impact of spontaneous cortical activity on PRF/GlyT2+ cells

208 Earlier data indicated that the activity of PRF/GlyT2+ cells can be linked to
209 different phases of slow cortical oscillations[23]. Here we asked to what extent the firing
210 activity of PRF/GlyT2+ cells is sensitive to the alterations of cortical states
211 (synchronized vs, desynchronized, Figures 4, S3A-C). We recorded PRF/GlyT2+
212 neurons (n=12) in GlyT2-eGFP transgenic animals and monitored the state changes
213 in LFP activity (Figure 4A-B). In the case of 7 cells, we recorded spontaneous state

214 changes between synchronized and desynchronized cortical states which can be
215 observed in light ketamine-xylazine anesthesia (Figure 4B) whereas in 5 cases we
216 evoked cortical inactivity by applying 2M potassium chloride (KCl) to the cortical
217 surface to induce cortical spreading depression (CSD, Figure S3D-F)[32].

218 In the first experiments, we observed that 5 out of 7 PRF/GlyT2+ cells fired
219 rhythmic AP clusters during the slow oscillatory periods (Figures 4B-D, S3A). When
220 the slow oscillation was replaced by a desynchronized period in the LFP, the firing
221 pattern of the PRF/GlyT2+ cells immediately followed this transition and became
222 irregular (Figures 4B-D, S3A). When the rhythmic cortical activity was restored, the AP
223 clusters reappeared (Figures 4B-D, S3C). The transition from rhythmic AP cluster to
224 tonic activity could be confirmed by autocorrelograms (Figures 4C, S3A). The mean
225 rate of PRF/GlyT2+ action potential clusters was significantly higher in synchronized
226 vs. desynchronized states (Figure 4D). The firing rate of PRF/GlyT2+ neurons
227 significantly increased during the desynchronized states (Figure S3B). In the CSD
228 experiments, cells decreased the rate of spike clusters upon cortical cell inactivation
229 (Figure S3F). These data demonstrate a tight connection between the cortical states
230 and firing activity of PRF/GlyT2 neurons and confirm the strong impact of the cortex
231 on these cells during spontaneous activity.

232 Co-innervation of PRF and the thalamic targets of PRF by L5 neurons

233 L5 neurons that innervate the striatum have been shown to arborize in the
234 thalamus[15,16] and since the basal ganglia also innervate the thalamus and thalamus
235 project back to the cortex the three structures form multiple nested loops[6,8,11].

236 To investigate if the same logic applies to individual L5 neurons targeting the
237 PRF i.e. whether L5 neurons simultaneously innervate PRF and the target region of

238 PRF/GlyT2+ cells in the thalamus (the intralaminar and parafascicular nuclei, IL/Pf)
239 we analyzed data from the Mouse Light Neuron Browser database[33]
240 (https://www.janelia.org/open-science/mouselight-neuronbrowser). In the database
241 we found 23 M2/Cg L5 neurons that had at least one axonal end point in the PRF
242 (Figure 5A-C; Table S1.). Seventy-four percent of these neurons (n=17) projected to
243 the IL/Pf as well. Ten out of the M2/Cg L5 17 neurons (59%) neurons co-innervating
244 PRF and IL/Pf displayed multiple axonal end points (here defined as more than 4 end
245 points) both in PRF and in the IL/PF. Four out of the 23 PRF projecting L5 neurons
246 (17.4%) displayed very dense axonal arbors in PRF (more than 10 axonal end points)
247 (Figure 5C). Three of these L5 cells innervated IL/Pf also with more than 10 axonal
248 end points. The fourth of them formed 6 end points in IL/Pf. Confirming our
249 anterograde tracing experiments, these neurons arborized more in the dorsomedial
250 part of the PRF (Figure 5C). These data suggest that co-innervation of PRF and IL/Pf
251 by individual cortical L5 neurons is common. Sixteen out of the 17 L5 neurons
252 (94.12%) co-innervating PRF and IL/Pf also had a collateral to the striatum indicating
253 that the cortico-PRF-thalamic message is projected to the basal ganglia as well (Table
254 S1).

255 The Mouse Light Neuron Browser data does not permit to establish whether the
256 cortico-PRF-thalamic neurons target PRF/GlyT2+ cells or other cell types in the PRF.
257 In order to demonstrate that thalamic-projecting cortical cells can innervate
258 PRF/GlyT2+ cells, we employed two experimental designs (Figures 5D and S4A). In
259 the first configuration, we injected AAVrg-EF1a-DIO-FlpO into the IL/Pf and AAV2/1-
260 EF1a-fDIO-mCherry into M2 in RPB4-Cre//GlyT2-eGFP mice (Figure 5D). In this case,
261 the Flp is Cre dependent, travels retrogradely from the thalamus to the cortex, and
262 expresses in RBP4+ L5 neurons (Figure 5E-F). The second virus is FLP-dependent

263 and travels anterogradely from those L5 neurons which project to the IL/Pf as well
264 (Figure 5G-K). In the second approach, we injected Cre-expressing retrograde virus
265 (AAVrg-EF1a-Cre) into the IL/Pf and AAV5-EF1a-DIO-hChR2-mCherry virus into the
266 M2 in GlyT2-EGFP mice (see more details in the Methods; Figure S4A).

267 In both experimental approaches, we observed retrogradely labeled deep layer
268 M2/Cg pyramidal cells (Figures 5F, S4B-C) and dense axonal arbor in the dorsolateral
269 Pf/IL verifying the injection sites and the thalamic projections (Figures 5G; S4D-H and
270 S4M-P). Dense cortical innervation was also observed in the PRF in every case (n=4
271 animals), in the same PRF/GlyT2+ area (Figures 5H-K, S4I-L), which we identified
272 after our original M2/Cg AAV5-DIO-ChR2-mCherry injections (as in Figure 1). The
273 cortical projection was largely ipsilateral in the PRF. Using high-resolution confocal
274 microscopy, we identified close appositions between axons of IL/Pf projecting cortical
275 neurons and the dendrites of PRF/GlyT2+ cells (Figure 5L-N). In the first experimental
276 configuration, 72.5% of PRF/GlyT2+ dendrites (n=40) were contacted by the axon
277 terminals of thalamic projecting M2/Cg axons, compared to 65% in the second
278 experiment (n=40). The mean number of close appositions per dendrite was 2.125 ±
279 0.308 in the first case and 1.45 ± 1.339 in the second. The pooled data show that 69%
280 of the PRF/GlyT2+ dendritic segments (n=80) were juxtaposed to M2/Cg boutons, with
281 an average of 1.45 ± 1.339 putative contacts per 50 μm segment (Figure 5O).
282 Together these data show that thalamus-projecting M2/Cg pyramidal cells can also
283 innervate PRF/GlyT2+ cells.

284 ## Activation of PRF/GlyT2+ neurons inhibit thalamocortical neuronal activity in
285 vivo

286 As the next step in the loop, we aimed to examine the impact of PRF/GlyT2+
287 activity on thalamic cells. PRF/GlyT2+ neurons have been shown to selectively
288 innervate IL/Pf and evoke non-depressing, mixed, GABA/glycine receptor-mediated
289 IPSCs on their targets[23]. However, the effect of this inhibitory input on the spike output
290 of IL/Pf has not been investigated. To address this, we performed in vivo juxtacellular
291 recording and labeling experiments in GlyT2-Cre mice injected with an AAV5-DIO-
292 ChR2-eYFP virus in the PRF (Figures 6 and S5). PRF/GlyT2+ fibers were then
293 photoactivated in the IL/Pf (Figure 6A-B). To ensure that the recorded IL/Pf neurons
294 were located within the PRF/GlyT2+ fibers, the position of the IL/Pf cells was
295 determined post hoc (Figure S5A). Given that IL/Pf neurons are known to be sensitive
296 to pain[34] we utilized urethane anesthesia to assess the impact of PRF/GlyT2+
297 photoactivation on spontaneous (n= 13 cells) as well as on tail-pinch-induced IL/Pf
298 activity (n= 10 cells, (Figures 6B-C, S5B-C). The stimulation frequency used (33 Hz)
299 was compatible with the spontaneous activity of PRF/GlyT2+ neurons measured
300 under identical conditions[23].

301 The baseline mean firing rate (MFR) of the recorded thalamic neurons (n=23)
302 varied between 1 and 30 Hz (Figure S5B). Tail pinch evoked a significantly higher
303 MFR in the IL/Pf cells (Figure S5B). Optogenetic activation of PRF/GlyT2+ fibers (33
304 Hz) in the IL/Pf resulted in a significant decrease of IL/Pf spiking activity in both
305 spontaneous and tail-pinch conditions at the population level (Figures 6B-C; S5C-D).
306 The firing rate immediately returned to baseline values upon the cessation of stimulus
307 trains (Figures 6B-C; S5C-D).

308 Nineteen out of the 23 IL/Pf neurons (82.6%) were considered strongly inhibited
309 (see Methods; Figure S5E). In these neurons, inhibition of the firing output increased
310 gradually and following a transient period of 1-2 seconds PRF/GlyT2+ inputs could
311 almost entirely block the firing output of IL/Pf cells (Figure S5D-E). In 9 neurons we
312 increased the duration of stimulation from 5 to 16 or 30 sec but the tonic cessation of
313 firing was maintained for the entire duration (n=9 cell, Figure S5D). Firing activity
314 returned to baseline levels after these long stimulations as well (Figure S5D). In the
315 case of 4 out of the 23 IL/Pf neurons (16.7%), the PRF/GlyT2+ activation resulted in a
316 brief gap (5-10 ms) in the PSTH immediately after the onset of the stimulus (Figure
317 S5F-G). The time course of this precisely timed inhibition corresponded well with the
318 kinetics of the fast GABAergic/glycinergic IPSCs recorded during the earlier in vitro
319 observations[23] indicating a fast, phasic inhibition in this subset of neurons. The activity
320 of control neurons in the thalamus, located outside the PRF/GlyT2+ projection zone
321 (n=5), was not altered by the activation of PRF/GlyT2+ fibers (Figure S5D, H).

322 The precise localization of IL/Pf neurons inhibited by PRF/GlyT2+ activation was
323 verified post hoc. IL/Pf cells were localized within the PRF/GlyT2+ fibers in all cases
324 (Figure S5A), mainly in the dorsolateral sectors. The recorded cells were distributed
325 both in the anterior (centrolateral and paracentral) and the posterior (parafascicular)
326 IL nuclei (Figure S5A). All weakly inhibited cells were localized in anterior IL. We
327 conclude that PRF/GlyT2+ neurons can exert a powerful effect on the spontaneous as
328 well as on tail pinch evoked firing activity of IL/Pf neurons and can participate in both
329 tonic (divisive) and phasic inhibition of IL/Pf outputs.

330 So far, we have shown that the cortico-PRF pathway can effectively control
331 PRF/GlyT2+ cells (Figures 3-4, S2-3) and that, in turn, PRF/GlyT2+ cells can strongly

332 inhibit their postsynaptic partner in the thalamus (Figures 6 and S5). However, it still
333 remains to directly demonstrate whether cortical L5 axons can actually target those
334 PRF/GlyT2+ neurons, which innervate the thalamus and inhibit IL/Pf neurons. To
335 investigate this question, we injected conditional retrograde AAVrg-hSyn-DIO-
336 mCherry virus into the IL/Pf and anterograde AAV5-CAMKIIa-hChR2-eYFP into the
337 M2/Cg of GlyT2-Cre mice (Figure 6D). We then examined the GlyT2+ cells
338 retrogradely labeled from the thalamus in the PRF and the M2/Cg terminals contacting
339 them. We confirmed the cortical injection sites in M2/Cg (Figure 6E) and their thalamic
340 projection in IL/Pf (Figure 6F-G). In the brainstem, we could frequently observe
341 retrogradely labeled PRF/GlyT2+ neurons among the cortical fibers (Figure 6H-K).
342 Using confocal microscopy, we confirmed M2/Cg terminals formed putative contacts
343 with 82% of all thalamus-projecting PRF/GlyT2+ dendrites (n=50, from 3 mice, Figure
344 6L-O). We calculated the mean number of close appositions in 50 μm long dendritic
345 segment, which was 2.4 ± 0.22 (Figure 6O).

346 These data identified cortical inputs on thalamic projecting PRF/GlyT2+ cells.
347 Together with the data showing that the same layer 5 cell can innervate PRF/GlyT2+
348 cells and IL/PF (Figure 5) and PRF/GlyT2+ cell contact IL/PF (Figure 6)[23] we
349 demonstrated that in this system cortex, PRF/GlyT2+ cells and thalamus can form
350 multiple nested loops.

351 Activation of PRF/GlyT2+ neurons promotes rotational movements

352 Next, we aimed to examine the behavioral effects of activating the thalamus
353 projecting PRF/GlyT2+ cells, a key node in the cortex-PRF-thalamus communication.
354 To address this, we injected AAV5-DIO-ChR2-eYFP into the PRF of GlyT2-Cre
355 animals and implanted fiber optics into the thalamus (IL/Pf) (n=7 stimulus site, n=2

356 animals). We then photoactivated PRF/GlyT2+ fibers unilaterally and bilaterally at
357 various laser intensities (Figure 7A) in IL/Pf. Bilateral stimulation (n=20 stimulation) or
358 unilateral stimulation with higher (15 mW) laser intensities (n=24 stim) resulted in
359 behavior arrest confirming earlier data[23]. Unilateral stimulation of PRF/GlyT2+ axons
360 in the IL/Pf at lower laser intensity (1, 5 and 10 mW), however, induced rotation always
361 in the contralateral direction (Figure 7B). Rotational movements significantly increased
362 during stimulation and decreased after stimulus termination (Figure 7B; Video S1).
363 Positions of the optic fibers were determined post hoc (Figure 7C).

364 These findings show that activation of thalamic projecting PRF/GlyT2+ cells via
365 their axons in IL/Pf consistently leads to contralateral rotation. However, not all
366 PRF/GlyT2+ cells may project to the thalamus. In order to identify, whether the
367 behavioral effect of activating thalamus projecting PRF/GlyT2+ cells differ from that of
368 the whole PRF/GlyT2+ population we injected AAV5-DIO-ChR2-eYFP into the PRF in
369 GlyT2-Cre animals and implanted fiber optics, now, into the PRF and photoactivated
370 PRF/GlyT2+ neurons unilaterally via their somata (Figure 7D) at various laser
371 intensities (1; 5; 10; 15 mW; 5 ms pulse with, 40 Hz for 10 sec, n=7 animals).

372 Since the effect of PRF/GlyT2+ soma activation on movement initiation and
373 maintenance has not been characterized first we measured the traveled distance in
374 the first second of the PRF/GlyT2+ stimulation and the subsequent 9 seconds (Figure
375 S6A). After the stimulus onset, we found significantly increased movement in the first
376 second of the stimulus relative to the baseline period (before stimulus) with 3
377 stimulation intensities (1, 10 mW) Figure S6A). Increased locomotion persisted in the
378 remaining 9 sec of the stimulation (Figure S6A). There was no significant dose-
379 response effect with increasing laser light intensity (Figure S6B).

380 Next, we examined rotational movements during the stimulation of PRF/GlyT2+
381 somata (10 sec) in the same animals (Figure 7E; Video S2-3). Calculated for the whole
382 population (n=7 optic fibers) rotational movements significantly increased compared
383 to the baseline periods upon optogenetic activation at all stimulation intensities (1, 5,
384 10 and 15 mW, Figure 7F). We found no significant dose-response effect with
385 increasing laser light intensity (Figure 7G). Interestingly, somatic stimulation of
386 PRF/GlyT2+ neurons induced contralateral rotational movements, similar to thalamic
387 stimulation of PRF/GlyT2+ fibers, in only 4 out of the 7 animals. In the remaining 3
388 animals ipsilateral rotation was observed (Figure 7H). We found no significant
389 differences in rotational angles between the ipsi- and contralaterally turning animals
390 (ipsi vs. contra stim for all intensity U=2 p=0.229). Post hoc histological identification
391 of optic fiber positions within the PRF revealed no discernible anteroposterior,
392 dorsoventral, or mediolateral differences between the animals exhibiting ipsi- or
393 contralateral rotational movements (Figure 7I, Figure S6C-D).

394 In the eYFP control animals, the mean traveled distance, and the rotational angle
395 was not significantly different between the baseline and stimulation periods (Figure
396 S6E-K, Video S4). Next, we conducted loss-of-function experiments by injecting
397 AAV5-DIO-eNpHR 3.0-eYFP into the PRF (n=4 animals) and implanting optic fibers
398 into the PRF (n=8 optic fibers, Figure S7A). Similar to the gain of function experiments
399 (Figures 7 and S6) we found that inhibition of PRF/GlyT2+ somata unilaterally could
400 result in both contra- and ipsiversive rotations (Figure S7C, Video S5). However, for
401 the whole group significant difference in rotational angles was not found (Figure S7C-
402 D). Movement initiation was significantly affected only at 15mW (Figure S7E-F).

403 These findings demonstrate that activation of PRF/GlyT2+ neurons can elicit
404 rotational movements. Activation of thalamic projecting PRF/GlyT2+ cells via their
405 axons elicits contralateral turning whereas activation of the entire PRF/GlyT2+ cells
406 population can evoke both ipsi- and contralateral turning.

407 ## Distinct projection patterns of thalamus projecting PRF/GlyT2+ cells

408 Next, we examined whether the observed differences in turning behavior
409 between PRF/GlyT2+ neurons innervating the thalamus and the entire PRF/GlyT2+
410 population can be explained by distinct projection patterns (Figure 8). We primarily
411 focused on the gigantocellular nucleus in the medulla (Gi) that has recently been
412 shown to be responsible for the motor commands of turning movements and
413 compared ipsi- and contralateral projections[1,10,21].

414 We investigated the output of thalamus projecting PRF/GlyT2+ cells by injecting
415 a retrograde Cre-dependent FlpO-containing virus (AAVrg-EF1a-DIO-FlpO) into the
416 IL/Pf thalamus and AAV2/1-EF1a-fDIO-mCherry (n=3) into the PRF in GlyT2-Cre mice
417 (Figure 8A1). This approach selectively labels the axon arbor of thalamus-projecting
418 PRF/GlyT2+ cells (Figures 8A, S8A-H). In order to label the axons from the entire
419 PRF/GlyT2+ population we injected AAV5-Ef1-DIO-eYFP into PRF of GlyT2-Cre
420 animals (n=4) (Figure 8B).

421 We found a stark difference in the innervation pattern of Gi between the two
422 approaches. Thalamus projecting PRF/GlyT2+ cells provided significantly more axons
423 to the ipsilateral Gi (Figure 8A5) whereas labeling the entire PRF/GlyT2+ population
424 resulted in ipsi- and contralateral axons in the Gi of similar density (Figure 8B5). In
425 addition, we found that thalamic-projecting PRF/GlyT2+ cells collateralized primarily
426 in the ipsilateral PRF whereas we observed substantial contralateral projection after

427 labeling the entire PRF/GlyT2+ population (Figure 8A2, B2). The thalamic projections
428 were mainly ipsilateral in both experimental approaches as described before[23] and
429 targeted the dorsolateral sector of Pf (Figure S8H-I) In addition, thalamus projecting
430 PRF/GlyT2+ cells innervated several other regions ipsilaterally including the basal
431 forebrain, hypothalamic regions, and the PAG which are not known to be involved in
432 turning behavior (Figure S8A-G) and are not contacted by thalamus projecting BG
433 cells[9]. These data indicate that thalamic projecting PRF/GlyT2+ cells form a specific
434 subpopulation of the PRF/GlyT2+ cells with a primarily ipsilateral projection pattern
435 that is distinct from the BG outputs.

436 Recent data have indicated that excitatory, vGLUT2-positive PRF cells project to
437 the contralateral Gi and are responsible for contraversive turning[10]. Our data, here,
438 however, demonstrate that a subpopulation of inhibitory PRF cells mainly project
439 ipsilaterally but still induce contraversive turning. In order to directly demonstrate the
440 difference between the projection pattern of excitatory and inhibitory PRF population
441 we utilized the fact that glycinergic cells are GABAergic as well[23,35] and used a double
442 transgenic vGAT-Flp//vGlut2-Cre mice to label both the excitatory and the inhibitory
443 projections in the same animals (Figures 8C, S8J). We co-injected AAVDj-EF1a-fDIO-
444 eYFP (cyan) and AAV5-hSyn-DIO-mCherry (magenta) unilaterally into the PRF
445 (Figure 8C-E) and examined the Gi (n=3). We could confirm that vGlut2+ neurons
446 provide significantly more axons to the contralateral Gi side as described before
447 (Figure 8C), while vGAT+ neurons project bilaterally (Figure 8D), with a significantly
448 higher fiber density on the ipsilateral side.

449 These experiments together confirm the presence of an inhibitory PRF cell
450 population that projects primarily to the ipsilateral Gi and activation of these cells can

451 have synergistic behavioral effects with the contraterally projecting excitatory PRF
452 neurons.

453 Discussion

454 Our data show that PRF/GlyT2+ cells are under strong cortical excitatory
455 influence and, in turn, are able to control the spiking activity of thalamic cells in the
456 IL/Pf. We demonstrate a loop-like organization between the cortex, PRF, and the
457 thalamus and show how the output from this loop can influence turning behavior via
458 the thalamus projecting PRF/GlyT2+ cells.

459 Multiple nested loops

460 If two brain centers are connected via a reciprocal loop and in addition there is a
461 third pathway that receives input from one of them and projects to the other, they form
462 nested loops[11]. Here, we have shown that besides the known reciprocal connectivity
463 between M2/Cg and IL/Pf[28,29], i; IL/Pf-projecting M2/Cg cells target PRF/GlyT2+ cells
464 (Figures 5 and S4), and ii; IL/Pf projecting PRF/GlyT2+ cells are among the targets of
465 M2/Cg neurons (Figure 6). We also show that M2/Cg cells target the same sector in
466 IL/Pf as the thalamus-projecting PRF/GlyT2+ cells. These anatomical data together
467 demonstrate a nested loop organization in the cortex-PRF-thalamus system.

468 In our functional assays, M2/Cg afferents evoked strong glutamatergic synaptic
469 responses in PRF/GlyT2+ cells both in vitro and in vivo (Figures 2-4). A particular
470 aspect of these experiments was that high-frequency activations of the afferents were
471 followed by faithful synaptic or spiking responses with little depression under both in
472 vitro and in vivo conditions. In addition, alterations of spontaneous cortical activity were
473 faithfully followed by a change in PRF/GlyT2+ firing patterns. In turn, the activation of

474 the thalamus-projecting PRF/GlyT2+ cells via their axons in the IL/Pf exerted
475 significant inhibitory action on their thalamic targets *in vivo* (Figure 6). Two types of
476 responses were distinguished, a gradual, tonic reduction in firing rate (divisive
477 inhibition) upon repetitive stimulation and the introduction of a brief gap, in the firing
478 activity following each stimulus (phasic inhibition). The inhibited thalamic neurons were
479 consistently found among the PRF/GlyT2+ fibers, providing morphological evidence
480 for a direct inhibitory action. The activity of thalamic cells outside the PRF/GlyT2+
481 axonal arborization areas remained unaffected by the stimulation. Earlier in vitro data
482 demonstrated non-depressing PRF/GlyT2+ IPSCs in IL/Pf cells upon repetitive
483 PRF/GlyT2+ stimulation[23]. This synaptic action may underlie the in vivo inhibitory
484 influence observed in this study. In summary, these data indicate that the indirect
485 pathway between M2/Cg and IL/Pf via the PRF/GlyT2+ cells is highly effective and
486 can modify the direct reverberating activity between the cortex and thalamus.

487 The cortex-PRF-thalamus loop is organized according to a similar basic logic to
488 the cortex-BG-thalamus loop. Both systems i; link interconnected cortical and thalamic
489 stations via an indirect inhibitory loop and ii; receive strong cortical excitation from L5
490 neurons which also project to the thalamus. Both BG and PRF provide powerful
491 inhibition to their thalamic targets[23,36–39] via large axon terminals that establish multiple
492 synapses on a single proximal dendritic target in the thalamus[23,40]. The major
493 difference between the two lies in the complexity of how the cortical input is processed
494 between the input and output stations.

495 Previous data suggested that linking interconnected thalamic and cortical regions
496 via an extrathalamic inhibitory transfer station which itself is under strong cortical
497 control, maybe a common organizing principle in sensory and motor systems[27]. Both

498 the anterior pretectal nucleus and the zona incerta have been shown to be under
499 strong cortical influence and to exert strong inhibition on the somatosensory thalamus
500 which itself receives powerful excitation from L5 of the primary somatosensory
501 cortex[41–43].

502 Our study demonstrated that most of the M2/Cg L5 pyramidal cells that
503 innervated IL/Pf and PRF/GlyT2+ neurons also provided collaterals to the striatum,
504 the input station of BG. IL/Pf is the target of both BG and PRF/GlyT2+ cells[23,29]. More
505 specifically, a recent study found that PRF-projecting SNR cells innervate the dorso-
506 lateral Pf/IL[9], the same region targeted by PRF/GlyT2+ cells (this study and[23]). This
507 indicates that despite the fact that BG and PRF/GlyT2+ cells do not interact directly[10]
508 they share the same cortical input pattern, and their output is integrated at the same
509 thalamic station, IL/Pf.

510 Both thalamic projecting SNR and PRF neurons distribute this message to many
511 other brain centers, but this projection pattern differs significantly. Target-specific
512 intersectional retrograde tracings demonstrated that SNR-thalamic neurons mainly
513 target the brainstem center involved in locomotion, orienting responses, orofacial and
514 muscle tone control. In contrast, our study shows that the PRF/GlyT2+ cells target
515 brain regions involved in emotional and motivational behavior, arousal, and fear
516 (Figure S8), with the exception of ipsilateral Gi (see below). This suggests that the two
517 loops are likely involved in different behavioral aspects of turning/orienting behavior.

518 ## Behavioral effects

519 Inhibition of IL/Pf cells via the activation of thalamus-projecting PRF/GlyT2+
520 neurons induced contralateral turning (Figure 7). This effect is consistent with the role
521 of IL/Pf in orienting behavior[25,26,44] particularly with its role in primarily ipsiversive

522 orientation[24]. However, the robust contralateral turning we observed here by activating
523 thalamus projecting axons in the IL/Pf suggests a direct motor effect via inhibition of
524 another brain center. Optogenetic activation of axons are known to propagate
525 antidromically and invade axon collaterals reaching other brain regions[45]. Examination
526 of the axonal arbor of thalamus-projecting PRF/GlyT2+ cells revealed only one output
527 station known to be involved directly in turning behavior, the Gi (Figures 8 and S8).
528 The presence of these descending collaterals confirmed earlier observations on a
529 PRF-Gi pattway[46,47]. Our study specifically demonstrated that while the entire
530 PRF/GlyT2+ cell population projects both to the ipsi- and contralateral Gi equally, the
531 thalamic projecting subpopulation exhibits a very strong bias toward the ipsilateral Gi.
532 Importantly, it is known that the inhibition of the reticulospinal, Chx10-expressing Gi
533 neurons results in contralateral turning whereas their activation has opposite
534 effect[20,21]. Thalamic projecting PRF/GlyT2+ neurons have a dual, GABAergic,
535 glycinergic phenotype and, as we show here, they can potently inhibit their targets
536 (Figures 6 and S5). Based on these we propose here that the contralateral turning
537 after the activation of thalamic projecting PRF/GlyT2+ cells arises primarily via the
538 inhibition of ipsilateral Gi through their descending collaterals. This is confirmed by the
539 fact that during contralateral turning, ipsilateral Gi cells are inhibited and display a
540 strong transient reduction in their activity[10]. Thus, based on our results, the
541 contralateral turning induced by activating thalamus-projecting inhibitory PRF/GlyT2+
542 cells is synergistic with the activation of excitatory PRF/vGLUT2+ cells[10]. In contrast
543 to thalamus-projecting PRF/GlyT2+ cells, PRF/vGLUT2+ cells project to the
544 contralateral Gi. Still their activation induce contralateral turning via the activation of
545 contralateral Chx10 expressing neurons (Fig 8 and [10]). Therefore, activation of PRF

546 can lead to contralateral turning both via a descending, ipsilateral, inhibitory pathway
547 and a descending, contralateral excitatory pathway to Gi.

548 As our data show, the activation of PRF may arise from the cortex and indeed
549 M2/Cg cortex has already been implicated in orchestrating orienting behavior [48–50].

550 In contrast to photoactivation of thalamus-projecting PRF/GlyT2 cells
551 contralateral turning could be elicited in only 4 out of the 7 animals following the
552 stimulation of PRF/GlyT2+ cell bodies. In 3 animals with PRF/GlyT2+ cell body
553 stimulation, ipsilateral, not contralateral rotation occurred suggesting a different
554 neuronal mechanism. Importantly, we did not find systematic differences in the
555 localization of the optic fibers inducing either ipsi- or contralateral rotation. In parallel
556 with these behavioral data, when we labeled the descending axons of the entire
557 PRF/GlyT2+ cell population to Gi we found no difference between the innervation of
558 ipsi- and contralateral sides. In contrast, there was a very strong ipsilateral bias when
559 we were labeling the thalamus-projecting PRF/GlyT2+ cells (see above). This
560 suggests the existence of a sizable non-thalamus-projecting PRF/GlyT2+ cell
561 population that innervates the contralateral side rather than the ipsilateral side.
562 Activating these cells would inhibit contralateral Gi, obviously leading to ipsilateral
563 turning. Thus, our data suggest that circuit elements responsible for ipsi- or
564 contralateral rotation in the PRF are intermingled. These results align well with recent
565 discoveries demonstrating the modularity or granularity of basal ganglia and brainstem
566 motor networks[2]. According to these findings, neuronal populations with specialized
567 functions in the brainstem can be located in close proximity and still coordinate
568 different types of motor program. Along these lines, it has been previously shown that

569 in the PRF, stimulation sites including unilateral or bilateral atonia via the spinal cord
570 are mixed in the PRF[19], indicating that granularity[2] may also apply to this region.

571 Open questions

572 Our study leaves several questions open for future investigations. First, many
573 cortical inputs were not in close apposition to PRF/GlyT2+ cells suggesting the
574 PRF/vGLUT2+ neurons might also be contacted. However, the direct synaptic input
575 and action of cortex on vGLUT2+ neurons remain to be established. Second, in
576 parallel with inhibitory PRF cells, vGLUT2+ PRF cells also provided input to the same
577 sector of IL/Pf (Figure S8). The role of this "push-pull" projection from PRF to the
578 thalamus requires further investigation. Finally, in contrast to the PRF/GlyT2+ labeling
579 that highlighted similar innervation of both sides of Gi equally, tracing PRF/vGAT+
580 cells revealed a strong ipsilateral bias in Gi (Figure 8D). Since all GlyT2+ cells are
581 vGAT+ as well[23] this finding suggests the presence of a sizable vGAT+/GlyT2- cell
582 population in the PRF that provides strong ipsilateral inhibition and thus can participate
583 in contralateral turning.

584 Conclusions

585 Our data show that cortical message arising from higher order motor cortices can be
586 processed parallelly by two distinct cortico-subcortical loops: the cortex-BG- thalamus
587 and the cortex-PRF-thalamus loops. The two systems have distinct output to the
588 brainstem still can have synergistic effects on turning behavior by targeting distinct
589 neuron populations in the PRF.

590

591

592 # STAR Methods

593 ## Animal housing

594 All experimental procedures were approved by the Institutional Ethical Codex,
595 Hungarian Act of Animal Care and Experimentation (1998, XXVIII, section 243/1998)
596 and the Institutional Animal Care and Use Committee of the Institute of Experimental
597 Medicine, Hungarian Research Network, Budapest and by the regulations of the
598 European Union guidelines (directive 2010/63/EU). The experiments were performed
599 by the National Animal Research Authorities of Hungary (PE/EA/877-7/2020). We
600 used healthy, adult male mice (40-150 days) for the experiments. We used the
601 following mice strains: GlyT2-Cre (Tg) - B6129F1 and Bl6Fx,
602 Rbp4/cre//BAC_glyt2/GFP (TgTg) - C57Bl/6J, vGAT/t2A-Flpo//BAC-vglut2/icre
603 (TmTg)-C57Bl/6J, BAC_glyt2/GFP -C57Bl/6J[29]. Mice were entrained in a 12-hour
604 light/dark cycle with food and water available as *ad libitum*. We performed animal
605 research according to the 3R principles.

606 ## Surgeries

607 Anesthesia

608 The surgeries were done for all experiments (anatomy, electrophysiology,
609 optogenetics) based on the following protocol. As anesthetics, mice received an
610 intraperitoneal injection of ketamine (111 mg/kg, Produlab Pharma, #07/01/2302) and
611 xylazine (4.3 mg/kg, Produlab Pharma, #07/03/2303). For the maintenance of the
612 anesthesia, intramuscular injection of ketamine/xylazine was given every 30-50 min
613 during the experiments. The head of the animal was fixed in a stereotaxic apparatus
614 (David Kopf Instruments, Tujunga, California 91042, Model 900 Small Animal

615 Stereotaxic Instrument). In one experimental condition, we used urethane anesthesia
616 during IL/Pf in vivo juxtacellular recordings (0.12–0.15 g/100 g).

617 Virus injections and fiber optics implantations

618 For the anatomical investigations and *in vitro* and *in vivo* electrophysiological
619 experiments, all stereotaxic tracer injections were performed using a glass pipette
620 (intraMARK, 20-30-µm tip diameter, BLAUBRAND, injection flow: 25nl/min) connected
621 to a syringe and a stereotaxic micromanipulator (Kopf Instruments). After injection, the
622 capillary was left at the injection site for 5-10 min before slow withdrawal to allow
623 diffusion and minimize backflow. The mice were perfused or were used for
624 experiments following a 3–6-week survival time.

625 For the investigation of the cortico L5-PRF pathway, we used
626 Rbp4/cre//BAC_glyt2/GFP (TgTg) mouse line (altogether n=25 mice)(n=11 for the
627 anatomical investigation, n=7 for *in vitro* electrophysiology and n=7 for *in vivo*
628 electrophysiology)

629 For all (in vivo and in vitro) electrophysiology and nine of the anatomical experiments
630 the following virus injection design was used. We injected
631 AAV5.EF1.dflox.hChR2(H134R)-mCherry.WPRE.hGH (based on Addgene plasmid
632 #20297, UNC Vector Core) cre-dependent virus into the frontal cortex, M2/Cg (AP:
633 Br.1 mm and 2 mm; ML: Br.0.5 mm; DV: 0.7 mm; bilaterally into 2-2 AP position, 80 nl
634 each, 4 injection/mouse). For *in vivo* electrophysiology L5 photoactivation, the optic
635 fibers (100 µm, 0.22 NA) were positioned above the virus injection site (M2/Cg).

636 For labeling the axon collaterals of PF targeting L5 neurons we used two types of virus
637 injection design (n=4), where in two caseswe injected AAVrg-EF1a-DIO-FlpO-WPRE-
638 HGHpA (Addgene #87306-AAVrg) virus into the Pf unilaterally (AP: -2, ML: 0,5, DV:

639 3; 30 nl) . After three weeks we injected AAV2/1-EF1a-fDIO-mCherry (Addgene
640 #114471-AAV2) virus into the M2/Cg (AP: Br.1 mm and 2 mm; ML: Br.0.5 mm; DV:
641 0.7 mm; unilaterally into 2 AP position, 80 nl each, 2 injection/mouse).

642 The other two cases we used BAC_glyt2/gfp mouse line (n=2) and we injected AAVrg-
643 EF1a-Cre (Addgene # 55636-AAVrg) into the Pf unilaterally (AP: -2, ML: 0,5, DV: 3;
644 30 nl). We waited three weeks and injected AAV5.EF1.dflox.hChR2(H134R)-
645 mCherry.WPRE.hGH (based on Addgene plasmid #20297, UNC Vector Core) into the
646 M2 (AP: Br.1 mm and 2 mm; ML: Br.0.5 mm; DV: 0.7 mm; unilaterally into 2 AP
647 position, 80 nl each, 2 injection/mouse).

648 The last experimental design of the cortico L5-PRF pathway's investigation was
649 labeling M2 axons on Pf-projecting PRF/GlyT+ neurons in GlyT2-Cre mice (n=4). We
650 injected AAV5-CAMKIIa-CHR2(H134R)-EYFP (Addgene #26969-AAV5) into the M2
651 (AP: Br.1 mm and 2 mm; ML: Br.0.5 mm; DV: 0.7 mm; unilaterally into 2 AP position,
652 80 nl each, 2 injection/mouse) and AAVrg-hSyn-DIO-mCherry (Addgene #50459-
653 AAVrg) into Pf unilaterally (AP: -2, ML: 0,5, DV: 3; 30 nl).

654 For the investigation of the PRF/GlyT2+-thalamic pathways altogether n=32 adult
655 GlyT2-Cre male mice were used including the in vivo optogenetic behavioral
656 (n=17),electrophysiology (juxtacellular recording, n=13) experiments and anatomical
657 investigation (n=3). For optogenetic activation of PRF/GlyT2+ cells, we injected
658 AAV5.EF1a.DIO.hChR2(H134R)-eYFP.WPRE.hGH (based on Addgene plasmid
659 #20298, UNC Vector Core).For optogenetic activation of PRF/GlyT2+ fibers in the
660 IL/Pf we did the same injections but bilaterally. For optogenetic inhibiton of the
661 PRF/GlyT2+ somata, we injected AAV5-Ef1a-DIO eNpHR 3.0-EYFP (Addgene
662 #26966-AAV5) into PRF bilaterally (AP:-4.4, ML:0.8, DV: 4.2, 100-100 nl). In the

663 control experiment we injected AAV5.EF1a.DIO.eYFP.WPRE.hGH (based on
664 Addgene plasmid #27056, Penn Core) virus into the PRF unilaterally (AP:-4.4, ML:0.8,
665 DV: 4.2, 100 nl).

666 After virus injection the optic fibers (Thorlabs, FG105UCA, Ø105 µm core, 0.22 NA)
667 were implanted into the PRF (n=15 optic fiber in n=11 mice, AP:-4.4, ML:0.8, DV: 4.2)
668 or IL/PF (n=7 optic fiber in n=2 mice, AP:-1.9 or 2.3 mm; ML: -0.8 mm; DV: -2.5 or -
669 2.8 mm). Mice recovered from surgery and the viruses could transfect the PRF/GlyT2+
670 cells for 3 weeks before behavioral testing or juxtacellular recording. The optic fibers
671 were labeled with DiI stain (1,1'-Dioctadecyl-3,3,3',3'-Tetramethylindocarbocyanine
672 Perchlorate ('DiI'; DiIC18(3); ThermoFisher Scientific, #D282).

673 For further investigation of the PRF/GlyT2+-thalamic pathways, we labeled the axon
674 arbors of PF targeting PRF/GlyT2+ cells (n=3 in GlyT2-Cre mice). We injected AAVrg-
675 EF1a-DIO-FlpO-WPRE-HGHpA (Addgene #87306-AAVrg) virus into the Pf
676 unilaterally (AP: -2, ML: 0,5, DV: 3; 30 nl). After three weeks we injected AAV1-EF1a-
677 fDIO-EYFP (Addgene #55641-AAV1) or AAV1-Ef1a-fDIO mCherry (Addgene
678 #114471-AAV1) into PRF unilaterally (AP:-4.4, ML:0.8, DV: 4.2, 100 nl).

679 For examining PRF/vGluT2+ and PRF/vGAT+ projections in the Gi we used
680 vGAT/t2A-Flpo//BAC-vglut2/icre mice (n=3). We injected mixed AAV5-hSyn-DIO-
681 mCherry (Addgene #50459-AAV5) and AAVDJ-EF1a-fDIO-EYFP-WPRE viruses
682 (based on Addgene plasmid #55641, UNC Vector Core) into the PRF unilaterally (AP:-
683 4.4, ML:0.8, DV: 4.2, 100 nl; 1:1 ratio of the viruses).

684

685 ## Histology

686 Perfusion and tissue fixation

687 Perfusions were performed under deep anesthesia (sodium pentobarbital 60 mg/kg).
688 Using saline and a fixative solution (0.1% glutaraldehyde (wt/vol) (Electron Microscopy
689 Sciences, #16210) and 4% paraformaldehyde (wt/vol) (TAAB Laboratory, #P001) in
690 0.1 PB. A peristaltic pump perfused the solutions through the ascending aorta. After
691 the fixation, the brain was sectioned using a vibratome (50 µm coronal slices).

692 Immunohistochemistry

693 For all immunostaining methods, we used TBS buffer. The sections were incubated in
694 sucrose solutions for cryoprotection and were frozen above liquid nitrogen to help the
695 penetration of the antibodies, followed by BSA treatment (4% 40 min). To visualize the
696 L5 fibers (ChR2-mCherry viral tracer) we used a rabbit anti-mCherry primary antibody
697 (1:4000 or 1:1000, BioVision, Inc., 23 California 95035, #5993-100, overnight). To
698 label GlyT2+ cells and fibers in the PRF and in the IL/Pf (in the case of eYFP containing
699 viral tracers or in the Rbp4/cre//BAC_glyt2/GFP mouse line), the sections were treated
700 with chicken anti-eGFP primary antibody (1:15000 or 1:1000, ThermoFisher,
701 #A10262).

702 For light and electron microscopic analysis when we visualized the L5 fibers in the
703 brainstem after the anti-mCherry primary antibody we used anti-rabbit ImmPRESS
704 (1:2, Vector Laboratories Burlingame, Ca 94010) and DAB-Ni/DAB (DAB-Ni: Nickel-
705 intensified 3,3′-diaminobenzidine (bluish-black reaction product), DAB: 3,3′-
706 diaminobenzidine, Sigma-Aldrich, #D5637, brown reaction product) as a chromogen.
707 In the other case, after the anti-eGFP primary antibody (1:15000, ThermoFisher,

708 #A10262) we used ABC (avidin biotinylated horseradish peroxidase complex, 1:300,
709 Vector Laboratories, #PK-4000) and DAB as a chromogen.

710 For fluorescent and confocal microscopic investigations of L5 fibers, after the anti-
711 mCherry primary antibody, we used Cy3-conjugated goat anti-rabbit secondary
712 antibody (1:500, Jackson Immunoresearch, RRID: AB_2313593; Code: 111-167-003)
713 or Cy3-conjugated donkey anti-rabbit (1:500, Jackson Immunoresearch, RRID:
714 AB_2307443; Code: 711-165-152). In the case of the anti-eGFP primary antibody, we
715 used the anti-chicken-Alexa488 secondary antibody (1:500, ThermoFisher, #A-11039)
716 or Alexa 488 donkey anti-chicken secondary antibody (1:500, Jackson
717 Immunoresearch, RRID: AB_2340375; Code: 703-545-155) to investigate
718 GlyT2//eGFP components.

719 After juxtacellular recordings neurobiotin was visualized with Cy3-conjugated
720 streptavidin (1:2000, Jackson Immunoresearch RRID: AB_2337244; Code: 016-160-
721 084) in the PRF or in the IL/Pf. The GlyT2+ neurons/fibers and the cortical axons were
722 visualized using the same histology mentioned above so we developed DAB-Ni/DAB
723 or fluorescent immunostaining respectively.

724 To localize the fiber optics and juxtacellularly labeled cells, check virus injections, and
725 analyze the fibers in the PRF, all micrographs were taken with OLYMPUS BX61,
726 FLUOVIEW FV1000 confocal microscopy (software: Olympus Fluoview 1.6) or with
727 ZEISS AxioPlan2 fluorescent microscopy with OLYMPUS DP70 camera (software:
728 Olympus DPController 1.2.1.108) or Zeiss Axio Imager M1 microscope coupled to an
729 AxioCam HrC digital camera.

730 Fluorescent microscopy

731 To verify virus expression and optic fiber placement, fluorescent images were captured
732 using a Panoramic Digital Slide Scanner (Zeiss, Plan-Apochromat 10X/NA 0.45, xy:
733 0.65 μm/pixel, Panoramic MIDI II; 3DHISTECH, Budapest, Hungary). Every sixth
734 section was stained and analyzed for each animal. Axonal projections in the Gi
735 originating from different cell populations in the PRF were quantified by delineating
736 regions of interest (ROIs) in the Gi (ipsilateral and contralateral, each 0.25 mm^2) based
737 on neuroanatomical landmarks identified using Hoechst counterstaining on
738 fluorescent images, which were delineated with SlideViewer software (3DHISTECH).

739 Axonal density analysis

740 For intensity density analysis, FIJI was used to split the color channels of each image
741 into red, green, and blue. The relevant channel (red for RFP, green for eGFP) was
742 converted to grayscale. Background noise was removed, and the 8-bit images were
743 then converted to binary with a consistent threshold for the reporter protein (RFP or
744 eGFP). This allowed for precise calculation of axonal density within the selected
745 regions. Axonal density in each image was calculated and expressed as the mean
746 area percentage. To compare the ipsilateral and contralateral axonal densities
747 statistically, the data were normalized to the ipsilateral side.

748 Density mapping analysis

749 Following fluorescent immunostaining, we investigated the density of L5 fibers in the
750 PRF. A map based on fiber density was created by FIJI software16[62]. A high-
751 magnification confocal micrograph was taken about PRF/GlyT2+ cells and M2/Cg L5
752 fibers (20x, NA: 0.75). The pictures were converted to 8-bit in depth then the brightest
753 pixels of single optical slices of the original image stacks were projected into one plane

754 to depict all of the labeled bright structures. These maximum intensity projections were
755 smoothed by a Gauss filter with a radius of 40 pixels then the pixels were ordered
756 according to their intensity values in 8 categories. The result is a pseudocolored, semi-
757 quantitative map of the fiber density that enables the localization of the highest fiber
758 density areas in a given image.

759 Confocal microscopy

760 Confocal images of the M2/Cg1, IL/Pf, and PRF regions were captured using a Nikon
761 C2 Confocal Laser Scanning Microscope. The imaging was performed with a 4x Plan
762 Fluor objective (NA 0.13, xy resolution 2 μm/pixel), a 10x Plan Fluor objective (NA
763 0.13, xy resolution 0.63 μm/pixel, z-step size 2 μm), and a 20x CFI Plan Apo VC
764 objective (NA 0.75, xy resolution 0.32 μm/pixel, z-step size 1 μm, Nikon Europe).
765 Confocal microscopy was used to analyze the spatial relationship between M2/Cg1
766 axonal boutons and labelled dendritic segments in the PRF. eYFP fluorescence was
767 amplified using anti-GFP labelling, and for close apposition analysis, RFP
768 fluorescence was amplified with anti-RFP labelling. To assess close appositions
769 between axonal boutons and dendritic segments in the PRF, high-resolution z-stack
770 images (Nikon CFI Plan Apo VC60X/NA 1.40 Oil objective, 0.09 μm/pixel, z-step size
771 0.3 μm) were taken from 5 μm of the slice. Confocal images were acquired with
772 consistent settings for pinhole size, gain level, axial section depth, and laser intensity
773 across all PRF slices. Close appositions, defined as potential synaptic contacts
774 between labeled axonal boutons and dendritic segments, were manually quantified
775 using NIS Elements Software. The analysis focused on identifying and counting
776 instances where eYFP- or RFP-labeled boutons were in close proximity to EGFP- or
777 RFP-labeled dendritic segments, indicating possible synaptic connections.

778 Electron microscopy

779 To analyze the M2/Cg terminals' ultrastructure, we performed immunostaining for the
780 ChR2-mCherry viral tracer (DAB, as described above). To confirm the innervation of
781 PRF/GlyT2+ neurons from M2/Cg, we performed double immunostaining for the
782 ChR2-mCherry viral tracer (DAB-Ni) and GlyT2+//eGFP (DAB) and processed the
783 material for EM. In our hands, the modified DAB-Ni precipitate in the axon terminals
784 could be unambiguously differentiated from the end product of marble-like DAB.

785 After double immunohistochemistry of L5 terminals and PRF/GlyT2+ cells the sections
786 were treated with OsO_4 (0.5%, vol/vol, with 7% sucrose for 40 min in 0.1 M PBS),
787 followed by dehydration, sequential incubation in ethanol, uranile acetate, and
788 acetonitrile for ultrastructural analysis. The dehydrated sections were embedded in
789 Durcupan (Sigma Aldricht, #44610Aldrich). Blocks containing PRF were re-embedded
790 and sectioned to ultrathin sections (60 nm thick) with an Ultramicrotome (EM UC6,
791 Leica Biosystems). The dendrites and terminals (area, diameter) were measured in
792 three non-consecutive sections in FIJI software[62].

793 The sections were examined using a HITACHI 7100 electron microscope; the electron
794 micrographs were taken with a Megaview digital camera.

795 In vitro electrophysiology

796 The *in vitro* electrophysiological experiments of Figure2 were performed on coronal
797 slices from the brains of PRF of adult mice (more than 3 months old), see the virus
798 injection method in the previous paragraph.

799 Slices were prepared for a minimum of 4 weeks following surgery. Briefly, mice were
800 anesthetized with an intraperitoneal injection of pentobarbital, then perfused through

801 the ascending aorta with cold (2°-5°C) bicarbonate-buffered saline (BBS) containing
802 (in mM): 115 NaCl, 2.5 KCl, 1.6 $CaCl_2$, 1.5 $MgCl_2$, 1.25 NaH_2PO_4, 26 $NaHCO_3$ and 30
803 glucose. Mice were then decapitated, and the portion of the brain containing the PRF
804 was extracted and placed in BBS at 2°-5°C for a few minutes. Slices (300 µm) were
805 then cut with a ceramic blade on a 7000smz-2 vibratome (Campden). The slicing
806 procedure was performed in an ice-cold solution containing (in mM): 130 potassium
807 gluconate, 15 KCl, 0.05 EGTA, 20 Hepes, 25 glucose, 1 $CaCl_2$ and 6 $MgCl_2$
808 supplemented with D-APV (50 µM). Slices were then transferred for a few minutes to
809 a solution containing (in mM): 225 d-mannitol, 2.5 KCl, 1.25 NaH_2PO_4, 25 $NaHCO_3$,
810 25 glucose, 1 $CaCl_2$ and 6 $MgCl_2$, and finally stored for the rest of the experimental
811 day at 32°-34° C in oxygenated BBS (pH 7.4 after equilibration with 95 % O_2 and 5 %
812 CO_2). For all recordings, slices were continuously superfused at 32°–34° C with
813 oxygenated BBS.

814 We recorded GFP-positive neurons from the pontine reticular formation (PRF; [29]). PRF
815 identification was facilitated by the presence of the red fluorescent plexus originating
816 from the cortical viral injections, observed via a 530 nm green LED (Thorlabs). Cells
817 were visualized with a combination of infrared Dodt contrast and an on-line video
818 contrast enhancement, using a CoolSnap HQ2 CCD camera (Photometrics) run by
819 MetaMorph (Universal Imaging). Fluorescent glycinergic neurons were identified using
820 a 470 nm-wavelength blue LED (Thorlabs). Both 470 nm and 530 nm LEDs were
821 coupled to the slice chamber via the epifluorescence pathway of the microscope.

822 Whole-cell, voltage clamp recordings were performed with an EPC-10 double amplifier
823 (Heka Elektronik) run by PatchMaster software (Heka). Patch pipettes (resistance 2-3
824 MΩ) were filled with an intracellular solution containing (mM): 110 $CsMeSO_3$ (Sigma),

825 4.6 $MgCl_2$, 10 HEPES, 10 K_2-creatine phosphate (Calbiochem), 10 TEA-Cl (Sigma),
826 0.05 4-AP (Sigma), 4 Na_2-ATP, 0.4 Na_2-GTP, 1 QX-314 (Tocris), pH 7.35 with CsOH
827 (~300 mOsm). Series resistance was partially compensated (max 65%), whereas
828 liquid junction potentials were not corrected. Stimulation train recordings were
829 performed at a holding potential of -60 mV. The AMPA and NMDA components of the
830 EPSCs were examined at both -60 mV, and +50 mV. The brief (2–3 ms long) flashes
831 of blue light used to evoke synaptic responses were provided by triggering the 470 nm
832 LED. TEA-Cl (500 μM) and 4-AP (50 μM) were added to the perfusing BBS when the
833 AMPA and NMDA components were investigated. This procedure was necessary both
834 for increasing synaptic release probability, and for reducing the sizeable current leaks
835 developing at +50 mV in control recording conditions, thus decisively improving EPSC
836 detection.

837 ## In vivo electrophysiology

838 Cortical activation and LFP recording

839 For in vivo investigation of the L5-PRF pathway we activated the M2/Cg L5 cells
840 optogenetically (see above the surgery details in Surgeriess n=7) and electrically (in
841 BAC_Glyt2/GFP mice, n=3). The laser beam was generated by a 473 nm laser
842 (Thorlabs lasers). The laser pulses were 5 ms long, 10 mW intensity, and were
843 delivered at 1,10 and 20 Hz frequencies (n=50 stimulus in 5 trains). When we applied
844 electrical stimulation (1-2 μA) we used a bipolar stimulating electrode on the surface
845 of the cortex (M2/Cg, same position described above).

846 To record cortical field potentials, bipolar LFP electrodes (FHC, resistance ~1 MΩ)
847 were inserted into the frontal cortex of mice (Bregma 1.7 mm; lateral -0.8 mm). The
848 recorded signal was amplified, band-pass filtered from 0.16 Hz to 5 kHz for LFP

849 recordings and from 100 Hz to 5 kHz to record the multiunit activity (Supertech
850 BioAmp, Supertech, Pécs, Hungary) and digitized at 20 kHz (micro 1401 MkII, CED,
851 Cambridge, UK).

852 Juxtacellular recording

853 PRF and IL/Pf single unit activity was recorded via glass microelectrodes (in vivo
854 impedance of 20-40 MΩ) made from borosilicate glass capillaries (1.5 mm outer
855 diameter, 0.75 or 0.86 inner diameters, Sutter Instrument Co., Novato, CA, USA or
856 WPI Inc. Sarasota, Fl, USA). Electrodes were positioned into the PRF (Bregma -4.4
857 mm; lateral -0.8 to -1 mm; ventral from cortical surface -3.8 to -4.8 mm) or IL/Pf
858 (Bregma -1.9 to 2.3 mm; lateral -0.8 mm; ventral from cortical surface -2.5 to -2.8 mm)
859 (using a piezoelectric microdrive (Burleigh 6000 ULN or ISS 8200, EXFO, Quebec
860 City, Quebec, Canada). Neuronal signals were amplified by a DC amplifier (Axoclamp
861 2B, Axon Instruments/Molecular Devices, Sunnyvale, CA, USA), further amplified, and
862 filtered between 0.16 Hz and 5 kHz by a signal conditioner (LinearAmp, Supertech)
863 and recorded by Spike2 5.0 (CED). The electrodes were filled with 0.5 M K+- acetate
864 and 2% neurobiotin (Vector Laboratories, Burlingame, CA, USA, #SP-1120).
865 Juxtacellular labeling of the recorded neurons was done by filling the neurons with
866 neurobiotin, as described in[37] . After the experiments, the animal was perfused, and
867 coronal sections were cut from the whole brain (3.1. Perfusion and tissue fixation). To
868 visualize neurons filled with neurobiotin and to determine their GlyT2 content (in the
869 PRF) or whether it is surrounded by PRF/GlyT2+ fibers (in IL/Pf), we treated the
870 sections as described in 3.2. Immunohistochemistry. The GlyT2::eGFP positivity was
871 determined by confocal microscopy.

872 Cortical spreading depression

873 The local application of 1M potassium chloride (KCl) or tetrodotoxin (sodium channel
874 inhibitor) induced CSD. The onset of cortical activity suppression happened after a few
875 minutes and lasted for 15-20 minutes. To facilitate the normalization of cortical activity
876 the cortical surface was rinsed with saline several times.

877 Janelia Mouse Light Neuron Browser

878 We analyzed single-cell reconstruction data of the Mouse Light Neuron Browser[40]
879 (https://www.janelia.org/open-science/mouselight-neuronbrowser) by identifying PRF
880 projecting M2/Cg L5 neurons, we selected neurons that have their soma in M2 or Cg
881 area and projected to the PRF. In the browser, we could set the threshold to the axonal
882 projection, called the in the browser “axonal endpoint”. We used 4 thresholds: >=10,
883 5-10, 2-5, or 1. We always precisely checked the anatomical region to uniform
884 terminology that we used during our research (Paxinos atlas vs Neuron Browser).

885 Behavior

886 Experimental protocol

887 After virus injection and optic fiber implantation (see above) the experimental protocol
888 included handling (2 weeks), habituation (3 days), and the optogenetic experiment.
889 The handling period started 1 week after the surgery. During the habituation, we
890 placed the mouse in the experimental box and connected their optic fiber to a fiber
891 optic patchcord (Thorlabs) and the patchcord cable (Thorlabs). The mice moved freely
892 in the experimental box and got used to the new environment and the weight of the
893 cable and the mouse was allowed to move passively. During the experiment phase,
894 we photoactivated or inhibited the transfected PRF/GlyT2+ cells or their fibers in IL/Pf.
895 The photoactivation was generated by a 473 nm DPSS laser (LRS-0473-PFM-00050-

896 03, Laserglow Technologies, Toronto, Canada). The photoinhibition was generated by
897 589 nm DPSS laser (LRS-0589-GFF-00100-05, Laserglow Technologies, Toronto,
898 Canada) The photostimulation trains were 10 s long, 5 ms light pulses at 40 Hz in PRF
899 every 1 minute in 4 laser intensities (1, 5, 10, 15 mW). The photoinhibiton trains were
900 10s long, and continuous stimulation. We stimulated every condition (every optic fiber)
901 20 times (5-5-5-5 stimulation by intensities), and the experiment took about 30 min.
902 During IL/Pf stimulation we used 30 Hz After the experiments, we perfused the animals
903 and identified the location of the virus injection and the optic fibers post hoc (see
904 Histology).

905 ## Analysis

906 In vitro analysis

907 Sampling frequency was 40 kHz. Data was filtered at 3 kHz. All data were analyzed
908 using routines developed in-house with Igor (Wavemetrics). Statistical comparisons
909 were performed using either the Mann-Whitney test for unpaired values, or the
910 Wilcoxon Signed-Rank test for paired sets of data, as indicated in the text. Statistical
911 significance was set at 0.05. Results are given as mean ± s.e.m.

912 Analysis for juxtacellular recordings

913 All statistical analysis was performed in R Statistical Computing Software (R Core
914 Team (2021). (R: A language and environment for statistical computing. R Foundation
915 for Statistical Computing, Vienna, Austria. URL https://www.R-project.org/).

916 PFC photoactivation

917 To evaluate the effect of photoactivation the first APs following each stimulus were
918 detected in a 40 ms window. They were distributed around ~10 ms peak with variable
919 spread. Only APs in the [25th percentile - 1.5*IQR, 75th percentile + 1.5*IQR] & AP

920 time > 0 ms range were considered evoked response. APs occurring outside of this
921 range were considered baseline firing activity and were excluded from further analysis.

922 Response probabilities were calculated as the number of evoked APs/number of
923 stimuli*100 and plotted alongside the median latency values.

924 Spontaneous frontal cortical activity changes

925 To determine synchronous and desynchronous periods the raw LFP signal was
926 filtered, down-sampled, and standardized. The power spectral density of each LFP
927 signal was calculated, and the dominant frequency was determined. To find the
928 synchronous and desynchronous periods of the cortical LFP signal, the standard
929 deviation of the signal amplitude was calculated in overlapping sliding windows. The
930 size of the sliding window was equal to the length of one cycle, and the overlap was
931 half a cycle. The threshold for synchronous and desynchronous periods was placed
932 halfway between the median and the 25th percentile.

933 The number of clusters was calculated in the synchronous and desynchronous periods
934 and was statistically compared using the Wilcoxon test. Action potential clusters were
935 determined by separating the two peaks at the minimum bimodal inter-spike interval
936 histograms (ISI). The number of bins of the ISI was determined by the Freedman-
937 Diaconis rule for optimal bin width; the window size was equal to the length of one
938 cycle of the slow cortical oscillation. The mean cluster rate per LFP state was
939 calculated by dividing the number of clusters by the length of the corresponding LFP
940 states in every recording.

941 The mean firing rate (MFR) was calculated by dividing the sum number of action
942 potentials divided by the sum lengths of the corresponding LFP states in every
943 recording.

944 Thalamocortical neuronal activity

945 MFR before, during, and after stimuli were calculated as the sum number of APs
946 divided by the sum length of each epoch. Based on the efficacy of the photo-
947 stimulation the cells were divided into *weak* and *strong inhibition* categories. If the ratio
948 of the number of APs +1s after and -1s before the stimulus was larger than 0.75
949 (number of spikes only dropped a little shortly after stimulus onset) the cell was
950 categorized as *weak*ly inhibited, if it was smaller than 0.75 (big drop of spike numbers
951 shortly after stimulus onset) the cell was categorized as *strong*ly inhibited.

952 Video analysis for behavior

953 To analyze the movements during the experiment we used Simple Mouse Tracker
954 (SMT) downloaded from GitHub. SMT is a video tracker software based on Open CV
955 that runs on any platform that supports Python. It is designed to track the body, head,
956 and tail coordinates (X, Y) of a single-colour mouse over a homogeneous color
957 background. https://github.com/joseaccruz/SimpleMouseTracker

958 After cleaning the tracking data (removing noise, outliers, and missing data) the
959 before-stimulus speed and rotation of the animals were compared to the during-
960 stimulus and -in the rotation experiments- to the after-stimulus periods.

961 To get the speed of the animals the Euclidean distance of the center (body) points
962 across every 5th frame was calculated and converted to mm (scaling factor: 1.6
963 mm/pixel). To get the rotation of the animal the signed angle of the body-head vector
964 was calculated across every frame and the mean rotation angles across frames were
965 plotted.

966 For traveled distance plots every 5th frame (data point) was used (25 fps, scale: 1.6
967 pixel/mm). We calculated distances and average speed (mm/sec) across every 5th

968 frame. Travelled distance (mm/sec) is averaged through the last second of the “before
969 stimulus” category and the first second of the stimulus and the last 9 seconds of the
970 stimulus. Travelled distance “after stimulus” is not included.

971 For rotation, we plotted every frame (data point). To show the animal’s movement
972 trajectory during stimuli the head-center-tail body points were plotted, separately in
973 non-stimulated and stimulated periods. We calculated vectors (based on head-body
974 X-Y coordination) and measured the mean angle changes of every vector. After that,
975 we multiplied that number with fps values and divided that number by 360 to get which
976 is the mean rotation angle during 1 sec relative to one whole circle. That value was
977 multiplied by 100 to obtain the percentage of rotation within 1 sec in relation to a
978 complete circle. The global angle threshold used in this file is 90. Grater rotation angles
979 between consecutive frames are replaced by zero.

980 Statistics

981 In all behavioral and electrophysiological experiments, mice were randomly assigned
982 to groups. Data points from animals with misplaced viral infections were excluded from
983 analysis. The number of animals used in each experiment is specified in the respective
984 figure legends. All data were checked for normality, and outliers were defined as
985 values outside the range of Q1 - 3*IQR and Q3 + 3*IQR. All statistical analyses were
986 performed using R Statistical Environment, Jamovi v 2.328, and Prism 8 software
987 (GraphPad Software). For the juxtacellular analysis, the following statistical methods
988 were applied: Mood's median test (two-sided), Wilcoxon Signed-Rank Test (one-sided
989 and two-sided, depending on the measure), and the Mann-Whitney test (two-sided).
990 In vitro analysis utilized the Wilcoxon Signed-Rank Test. Behavioral data were
991 analyzed using Friedman ANOVA with the Durbin-Conover post-hoc test, Wilcoxon

Signed-Rank Test (one-sided), and the Mann-Whitney test (two-sided). Ipsilateral and contralateral axonal projection density was analyzed using a two-sided paired t-test.

Data Availability

All relevant data supporting the findings of this study are available within the article and its supplementary materials. Additionally, source data and codes will be deposited in an appropriate public structured data repositories to ensure accessibility and future use.

Full access to the data will be granted upon publication to enable comprehensive assessment and validation of our results. In compliance with our commitment to open science, we are prepared to provide full access to the data, should it be required for the peer review.

Acknowledgement

We thank the Light Microscopy Center, the Electron Microscopy Center and the Virus Technology Unit at the Institute of Experimental Medicine for providing support for the experiments. Authors would like to thank Krisztina Faddi for their excellent technical assistance and to Csaba Dávid for his help in quantifying the cortical input density in PRF.

Funding

ERC Advanced Grant FRONTHAL, 742595 (LA)

European Union project within the framework of the Artificial Intelligence National Laboratory RRF-2.3.1-21-2022-00004 (LA)

Hungarian Academy of Sciences – “Lendület” Program LP2023-2/2023 (LA)

Author contributions

Conceptualization: EB, VP, LB, LA

Methodology: EB, VP, MAD, LB, KK, LA

Investigation: EB, VP, MAD, LB, KK

Visualization: EB, VP, LB

Funding acquisition: MAD, LA

Project administration: LA

Supervision: LA

Writing – original draft: EB, MAD, VP, LB, LA

References

1. Leiras, R., Cregg, J.M., and Kiehn, O. (2022). Brainstem Circuits for Locomotion. Annu Rev Neurosci *45*, 63–85. https://doi.org/10.1146/ANNUREV-NEURO-082321-025137.

2. Arber, S., and Costa, R.M. (2022). Networking brainstem and basal ganglia circuits for movement. Nature Reviews Neuroscience 2022 23:6 *23*, 342–360. https://doi.org/10.1038/s41583-022-00581-w.

3. Smith, Y., Raju, D. V., Pare, J.F., and Sidibe, M. (2004). The thalamostriatal system: A highly specific network of the basal ganglia circuitry. Preprint at Trends Neurosci, https://doi.org/10.1016/j.tins.2004.07.004 https://doi.org/10.1016/j.tins.2004.07.004.

4. Cui, G., Jun, S.B., Jin, X., Pham, M.D., Vogel, S.S., Lovinger, D.M., and Costa, R.M. (2013). Concurrent activation of striatal direct and indirect pathways during action initiation. Nature *494*, 238–242. https://doi.org/10.1038/nature11846.

5. Díaz-Hernández, E., Contreras-López, R., Sánchez-Fuentes, A., Rodríguez-Sibrían, L., Ramírez-Jarquín, J.O., and Tecuapetla, F. (2018). The Thalamostriatal Projections Contribute to the Initiation and Execution of a Sequence of Movements. https://doi.org/10.1016/j.neuron.2018.09.052.

6. Foster, N.N., Barry, J., Korobkova, L., Garcia, L., Gao, L., Becerra, M., Sherafat, Y., Peng, B., Li, X., Choi, J.H., et al. (2021). The mouse cortico–basal ganglia–thalamic network. Nature *598*, 188. https://doi.org/10.1038/S41586-021-03993-3.

7. Hintiryan, H., Foster, N.N., Bowman, I., Bay, M., Song, M.Y., Gou, L., Yamashita, S., Bienkowski, M.S., Zingg, B., Zhu, M., et al. (2016). The mouse cortico-striatal projectome. Nature Neuroscience 2016 19:8 *19*, 1100–1114. https://doi.org/10.1038/nn.4332.

8. Alexander, G.E., DeLong, M.R., and Strick, P.L. (2003). Parallel Organization of Functionally Segregated Circuits Linking Basal Ganglia and Cortex. https://doi.org/10.1146/annurev.ne.09.030186.002041 *VOL. 9*, 357–381. https://doi.org/10.1146/ANNUREV.NE.09.030186.002041.

9. McElvain, L.E., Chen, Y., Moore, J.D., Brigidi, G.S., Bloodgood, B.L., Lim, B.K., Costa, R.M., and Kleinfeld, D. (2021). Specific populations of basal ganglia output neurons target distinct brain stem areas while collateralizing throughout the diencephalon. Neuron *109*, 1721-1738.e4. https://doi.org/10.1016/J.NEURON.2021.03.017.

10. Cregg, J.M., Sidhu, S.K., Leiras, R., and Kiehn, O. (2024). Basal ganglia–spinal cord pathway that commands locomotor gait asymmetries in mice. Nature Neuroscience 2024 27:4 *27*, 716–727. https://doi.org/10.1038/s41593-024-01569-8.

11. Acsády, L. (2023). Heterogeneity of Thalamic Input Landscapes. The Cerebral Cortex and Thalamus, 32–44. https://doi.org/10.1093/MED/9780197676158.003.0004.

12. Jaramillo, J., and Guo, Z. V. (2023). Thalamocortical Contributions to Neural Dynamics and Behavior. The Cerebral Cortex and Thalamus, 367–380. https://doi.org/10.1093/MED/9780197676158.003.0035.

1071 13. McNaughton, N., and Vann, S.D. (2022). Construction of complex memories via
1072 parallel distributed cortical-subcortical iterative integration. Trends Neurosci *45*,
1073 550. https://doi.org/10.1016/J.TINS.2022.04.006.

1074 14. Berendse, H.W., and Groenewegen, H.J. (1990). Organization of the
1075 thalamostriatal projections in the rat, with special emphasis on the ventral
1076 striatum. J Comp Neurol *299*, 187–228.
1077 https://doi.org/10.1002/CNE.902990206.

1078 15. Pare, D., and Smith, Y. (1996). Thalamic Collaterals of Corticostriatal Axons:
1079 Their Termination Field and Synaptic Targets in Cats. J Comp Neurol, 372–551.
1080 https://doi.org/10.1002/(SICI)1096-9861(19960902)372:4.

1081 16. Levesque, M., Gagnon, S., Parent, A., and Deschenes (1996). Axonal
1082 arborizations of corticostriatal and corticothalamic fibers arising from the second
1083 somatosensory area in the rat. Cereb Cortex *6*, 759-70.

1084 17. Economo, M.N., Viswanathan, S., Tasic, B., Bas, E., Winnubst, J., Menon, V.,
1085 Graybuck, L.T., Nguyen, T.N., Smith, K.A., Yao, Z., et al. (2018). Distinct
1086 descending motor cortex pathways and their roles in movement. Nature *563*,
1087 79–84. https://doi.org/10.1038/s41586-018-0642-9.

1088 18. Mileykovskiy, B.Y., Kiyashchenko, L.I., Kodama, T., Lai, Y.Y., and Siegel, J.M.
1089 (2000). Activation of Pontine and Medullary Motor Inhibitory Regions Reduces
1090 Discharge in Neurons Located in the Locus Coeruleus and the Anatomical
1091 Equivalent of the Midbrain Locomotor Region. Journal of Neuroscience *20*,
1092 8551–8558. https://doi.org/10.1523/JNEUROSCI.20-22-08551.2000.

1093 19. Hajnik, T., Lai, Y.Y., and Siegel, J.M. (2000). Atonia-Related Regions in the
1094 Rodent Pons and Medulla. J Neurophysiol *84*, 1942.
1095 https://doi.org/10.1152/JN.2000.84.4.1942.

1096 20. Goñi-Erro, H., Selvan, R., Caggiano, V., Leiras, R., and Kiehn, O. (2023).
1097 Pedunculopontine Chx10+ neurons control global motor arrest in mice. Nature
1098 Neuroscience 2023, 1–13. https://doi.org/10.1038/s41593-023-01396-3.

1099 21. Cregg, J.M., Leiras, R., Montalant, A., Wanken, P., Wickersham, I.R., and Kiehn,
1100 O. (2020). Brainstem neurons that command mammalian locomotor
1101 asymmetries. Nat Neurosci *23*, 730–740. https://doi.org/10.1038/S41593-020-
1102 0633-7.

1103 22. Zeilhofer, H.U., Studler, B., Arabadzisz, D., Schweizer, C., Ahmadi, S., Layh, B.,
1104 Bösl, M.R., and Fritschy, J.M. (2005). Glycinergic neurons expressing enhanced
1105 green fluorescent protein in bacterial artificial chromosome transgenic mice. J
1106 Comp Neurol *482*, 123–141. https://doi.org/10.1002/CNE.20349.

1107 23. Giber, K., Diana, M.A., M Plattner, V., Dugué, G.P., Bokor, H., Rousseau, C. V,
1108 Maglóczky, Z., Havas, L., Hangya, B., Wildner, H., et al. (2015). A subcortical
1109 inhibitory signal for behavioral arrest in the thalamus. Nat Neurosci *18*, 562–568.
1110 https://doi.org/10.1038/nn.3951.

1111 24. Fallon, I.P., Hughes, R.N., Severino, F.P.U., Kim, N., Lawry, C.M., Watson,
1112 G.D.R., Roshchina, M., and Yin, H.H. (2023). The role of the parafascicular
1113 thalamic nucleus in action initiation and steering. Current Biology *33*, 2941-
1114 2951.e4. https://doi.org/10.1016/j.cub.2023.06.025.

1115 25. Matsumoto, N., Minamimoto, T., Graybiel, A.M., and Kimura, M. (2001).
1116 Neurons in the thalamic CM-Pf complex supply striatal neurons with information
1117 about behaviorally significant sensory events. J Neurophysiol *85*, 960–976.
1118 https://doi.org/10.1152/jn.2001.85.2.960.

1119 26. Minamimoto, T., and Kimura, M. (2002). Participation of the thalamic CM-Pf
1120 complex in attentional orienting. J Neurophysiol *87*, 3090–3101.
1121 https://doi.org/10.1152/JN.2002.87.6.3090.

1122 27. Halassa, M.M., and Acsády, L. (2016). Thalamic Inhibition: Diverse Sources,
1123 Diverse Scales. Trends Neurosci *39*. https://doi.org/10.1016/j.tins.2016.08.001.

1124 28. Gonzalo-Martín, E., Alonso-Martínez, C., Sepúlveda, L.P., and Clasca, F.
1125 (2023). Micropopulation mapping of the mouse parafascicular nucleus
1126 connections reveals diverse input–output motifs. Front Neuroanat *17*, 1305500.
1127 https://doi.org/10.3389/FNANA.2023.1305500/BIBTEX.

1128 29. Van der Werf, Y.D., Witter, M.P., and Groenewegen, H.J. (2002). The
1129 intralaminar and midline nuclei of the thalamus. Anatomical and functional
1130 evidence for participation in processes of arousal and awareness. Brain Res
1131 Brain Res Rev *39*, 107–140.

1132 30. Harris, J.A., Mihalas, S., Hirokawa, K.E., Whitesell, J.D., Choi, H., Bernard, A.,
1133 Bohn, P., Caldejon, S., Casal, L., Cho, A., et al. (2019). Hierarchical organization
1134 of cortical and thalamic connectivity. Nature *575*, 195–202.
1135 https://doi.org/10.1038/S41586-019-1716-Z.

1136 31. Pinault, D. (1996). A novel single-cell staining procedure performed in vivo under
1137 electrophysiological control: Morpho-functional features of juxtacellularly labeled

1138 thalamic cells and other central neurons with biocytin or Neurobiotin. J Neurosci
1139 Methods *65*, 113–136. https://doi.org/10.1016/0165-0270(95)00144-1.

1140 32. Groh, A., Bokor, H., Mease, R.A., Plattner, V.M., Hangya, B., Stroh, A.,
1141 Deschenes, M., and Acsády, L. (2014). Convergence of cortical and sensory
1142 driver inputs on single thalamocortical cells. Cereb Cortex *24*, 3167–3179.
1143 https://doi.org/10.1093/CERCOR/BHT173.

1144 33. Economo, M.N., Clack, N.G., Lavis, L.D., Gerfen, C.R., Svoboda, K., Myers,
1145 E.W., and Chandrashekar, J. (2016). A platform for brain-wide imaging and
1146 reconstruction of individual neurons. Elife *5*.
1147 https://doi.org/10.7554/ELIFE.10566.

1148 34. Arnts, H., Coolen, S.E., Fernandes, F.W., Schuurman, R., Krauss, J.K.,
1149 Groenewegen, H.J., Van Den Munckhof, P., and Arnts, H. (2023). The
1150 intralaminar thalamus: a review of its role as a target in functional neurosurgery.
1151 Brain Commun. https://doi.org/10.1093/BRAINCOMMS/FCAD003.

1152 35. Jonas, P., Bischofberger, J., and Sandkühler, J. (1998). Corelease of two fast
1153 neurotransmitters at a central synapse. Science (1979) *281*, 419–424.
1154 https://doi.org/10.1126/SCIENCE.281.5375.419/ASSET/0862CACE-9829-
1155 4AD4-B325-DD558F0D29F9/ASSETS/GRAPHIC/SE2986687005.JPEG.

1156 36. Ueki, A. (1983). The mode of nigro-thalamic transmission investigated with
1157 intracellular recording in the cat. exp brain res *49*, 116–124.

1158 37. Chevalier, G., and Deniau, J.M. (1982). Inhibitory nigral influence on cerebellar
1159 evoked responses in the rat ventromedial thalamic nucleus. Exp Brain Res *48*,
1160 369–376. https://doi.org/10.1007/BF00238613.

1161 38. Goldberg, J.H., Farries, M.A., and Fee, M.S. (2013). Basal ganglia output to the
1162 thalamus: still a paradox. Trends Neurosci *36*, 695–705.
1163 https://doi.org/10.1016/J.TINS.2013.09.001.

1164 39. Anderson, M.E., Postupna, N., and Ruffo, M. (2003). Effects of high-frequency
1165 stimulation in the internal globus pallidus on the activity of thalamic neurons in
1166 the awake monkey. J Neurophysiol *89*, 1150–1160.
1167 https://doi.org/10.1152/JN.00475.2002/ASSET/IMAGES/LARGE/9K0232850110
1168 .JPEG.

1169 40. Bodor, Á.L., Giber, K., Rovó, Z., Ulbert, I., and Acsády, L. (2008). Structural
1170 correlates of efficient GABAergic transmission in the basal ganglia-thalamus
1171 pathway. Journal of Neuroscience *28*.
1172 https://doi.org/10.1523/JNEUROSCI.5266-07.2008.

1173 41. Barthó, P., Freund, T.F., and Acsády, L. (2002). Selective GABAergic
1174 innervation of thalamic nuclei from zona incerta. Eur J Neurosci *16*, 999–1014.

1175 42. Barthó, P., Slézia, A., Varga, V., Bokor, H., Pinault, D., Buzsáki, G., and Acsády,
1176 L. (2007). Cortical Control of Zona Incerta. The Journal of Neuroscience *27*,
1177 1670. https://doi.org/10.1523/JNEUROSCI.3768-06.2007.

1178 43. Bokor, H., Frere, S.G., Eyre, M.D., Slezia, A., Ulbert, I., Luthi, A., and Acsady,
1179 L. (2005). Selective GABAergic control of higher-order thalamic relays. Neuron
1180 *45*, 929–940.

1181 44. Kinomura, S., Larsson, J., Gulyás, B., and Roland, P.E. (1996). Activation by
1182 Attention of the Human Reticular Formation and Thalamic Intralaminar Nuclei.
1183 Science (1979) *271*, 512–515. https://doi.org/10.1126/SCIENCE.271.5248.512.

1184 45. Mátyás, F., Komlósi, G., Babiczky, Á., Kocsis, K., Barthó, P., Barsy, B., Dávid,
1185 C., Kanti, V., Porrero, C., Magyar, A., et al. (2018). A highly collateralized
1186 thalamic cell type with arousal-predicting activity serves as a key hub for graded
1187 state transitions in the forebrain. Nat Neurosci *21*, 1551–1562.
1188 https://doi.org/10.1038/s41593-018-0251-9.

1189 46. Gallager, D.W., and Pert, A. (1978). Afferents to brain stem nuclei (brain stem
1190 raphe, nucleus reticularis pontis caudalis and nucleus gigantocellularis) in the
1191 rat as demonstrated by microiontophoretically applied horseradish peroxidase.
1192 Brain Res *144*, 257–275. https://doi.org/10.1016/0006-8993(78)90153-1.

1193 47. Hermann, D.M., Luppi, P.H., Peyron, C., Hinckel, P., and Jouvet, M. (1997).
1194 Afferent projections to the rat nuclei raphe magnus, raphe pallidus and reticularis
1195 gigantocellularis pars α demonstrated by iontophoretic application of
1196 choleratoxin (subunit b). J Chem Neuroanat *13*, 1–21.
1197 https://doi.org/10.1016/S0891-0618(97)00019-7.

1198 48. Erlich, J.C., Bialek, M., and Brody, C.D. (2011). A cortical substrate for memory-
1199 guided orienting in the rat. Neuron *72*, 330–343.
1200 https://doi.org/10.1016/j.neuron.2011.07.010.

1201 49. Hanks, T.D., Kopec, C.D., Brunton, B.W., Duan, C.A., Erlich, J.C., and Brody,
1202 C.D. (2015). Distinct relationships of parietal and prefrontal cortices to evidence
1203 accumulation. Nature 2015 520:7546 *520*, 220–223.
1204 https://doi.org/10.1038/nature14066.

1205 50. Brecht, M. (2011). Movement, Confusion, and Orienting in Frontal Cortices.
1206 Neuron *72*, 193–196. https://doi.org/10.1016/J.NEURON.2011.10.002.

Graphical abstract

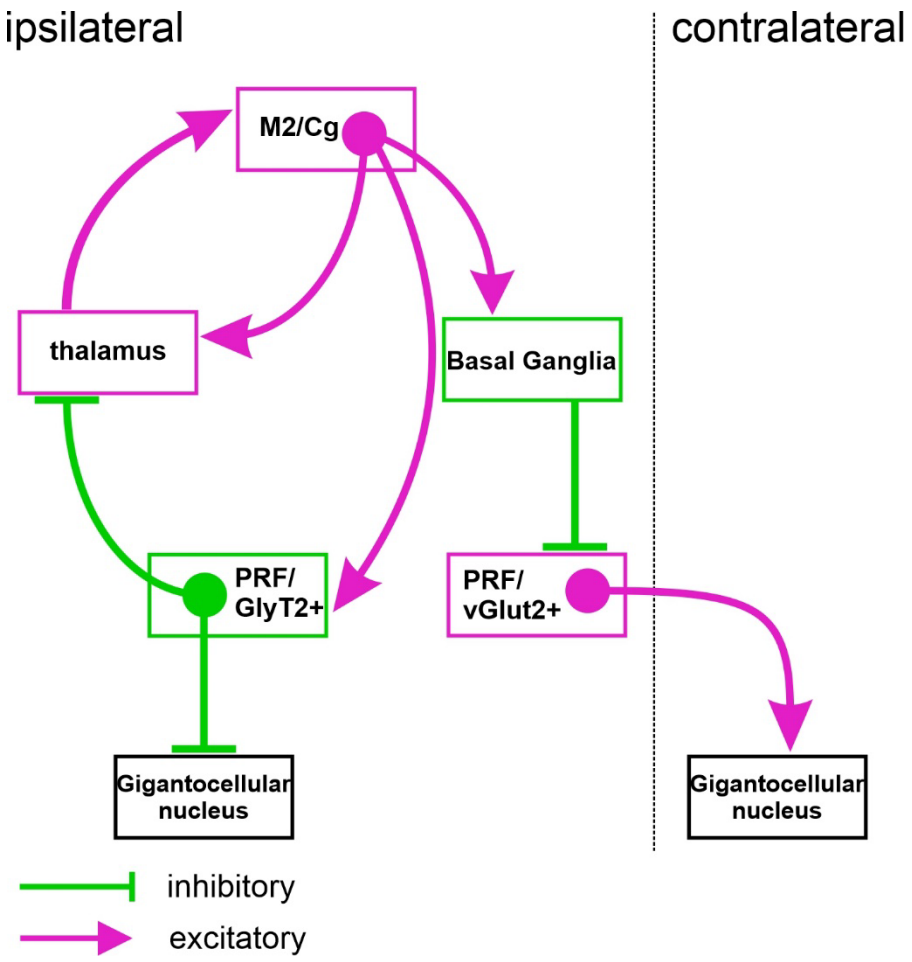

Main figures

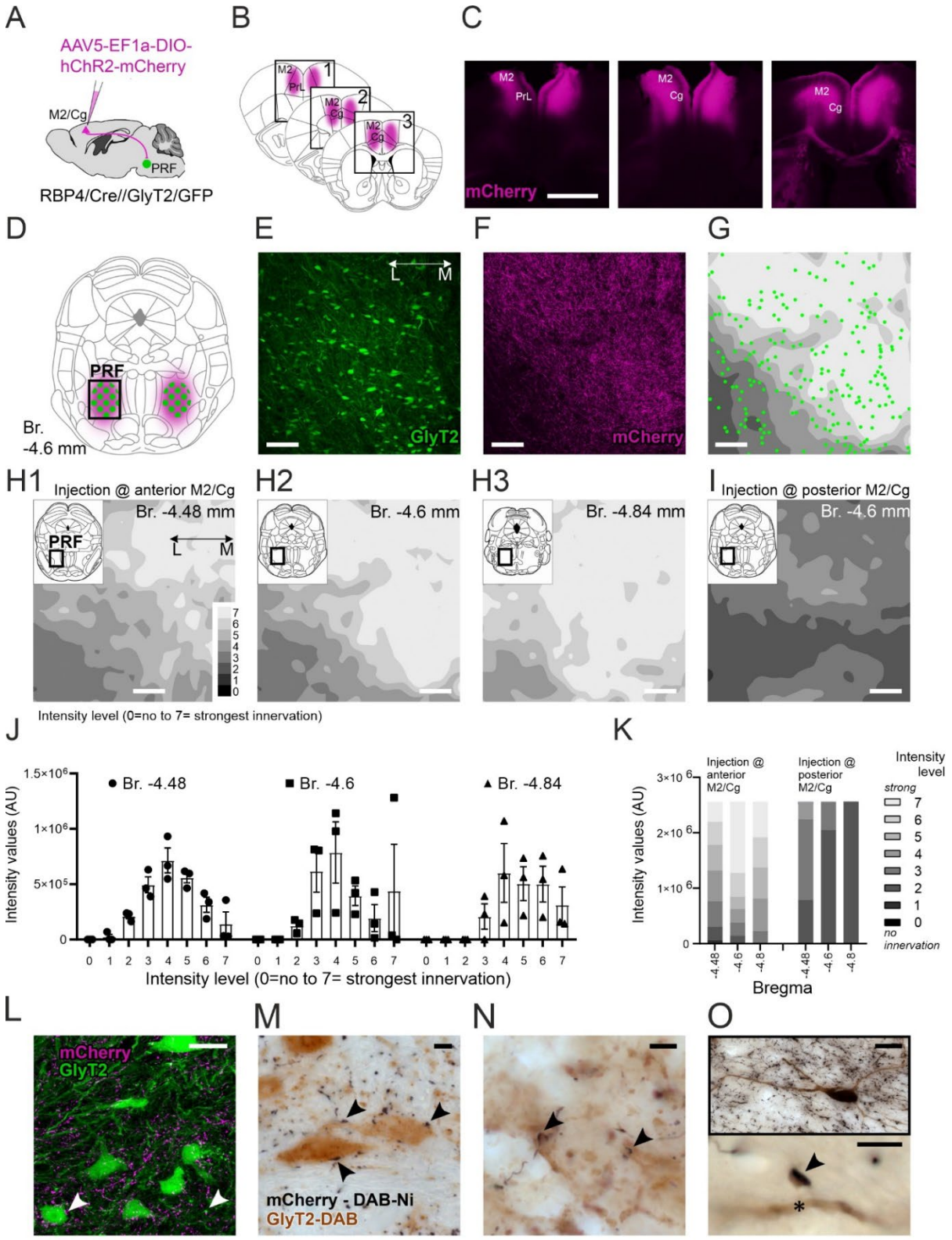

1213 Figure 1: Cortical inputs to PRF/GlyT2+ cells.

1214 A) Scheme of anterograde tracing from the frontal cortical motor-related areas (M2/Cg)
1215 in the RBP4-Cre//GlyT2-eGFP mouse line (n=9 mice).

1216 B) Schematic view of the injection sites.

1217 C) Low-power fluorescent micrographs of the cortical injection sites at three
1218 anteroposterior levels.

1219 D) Schematic view of the M2/Cg fibers (magenta shade) and PRF/GlyT2+ cells (green
1220 dots). The black rectangle, the position of the micrographs and heatmaps in e-g.

1221 E-F) Confocal micrographs (n=5 mice) of the glycinergic cells (E) and anterogradely
1222 labeled M2/Cg cortical fibers (F) in the PRF glycinergic zone.

1223 G) Fiber density heat map showing the distribution of cortical fibers (grey shading) and
1224 PRF/GlyT2+ cells (green dots). Higher fiber density is indicated with light grey colors.

1225 H1-3) Maximum intensity Z projections of average cortical fiber heat maps (n=3
1226 animals) showing anterior M2/Cg inputs at three anteroposterior PRF levels extending
1227 from Br. -4.6 to Br. -4.84 (from the Paxinos atlas; 250µm)

1228 I) Maximum intensity Z projections of cortical fiber heat maps (n=3 animals) showing
1229 posterior M2/Cg inputs.

1230 J) Quantitative analysis of the anterior M2/Cg fibers in the PRF at three coronal levels.
1231 Intensity levels represent fiber density values between 0 and 7. Where 0 indicates no
1232 innervation and 7 presents the strongest innervation.

1233 K) Proportion of innervation densities in the PRF after anterior (left) and posterior
1234 (right) M2/Cg injections at three coronal levels.

1235 L) High power confocal fluorescent image of anterogradely labeled M2/Cg fibers
1236 (magenta) and PRF/GlyT2+ neurons (60x, n=5 mice)

1237 M-O) High power light microscopic image (n=9 mice) of close apposition between
1238 M2/Cg fibers (black) and the somata (k), dendrites (l), or a spine (m) of PRF/GlyT2+
1239 neurons. Inset in m displays the juxtacellularly labeled PRF/GlyT2+ cell; arrowheads,
1240 cortical inputs; asterisk, and spine.
1241 Scale bars: c) 1 mm; e-i) 100 µm; j) 20 µm; k-l) 5 µm; m) 5µm, 20µm in the inset.

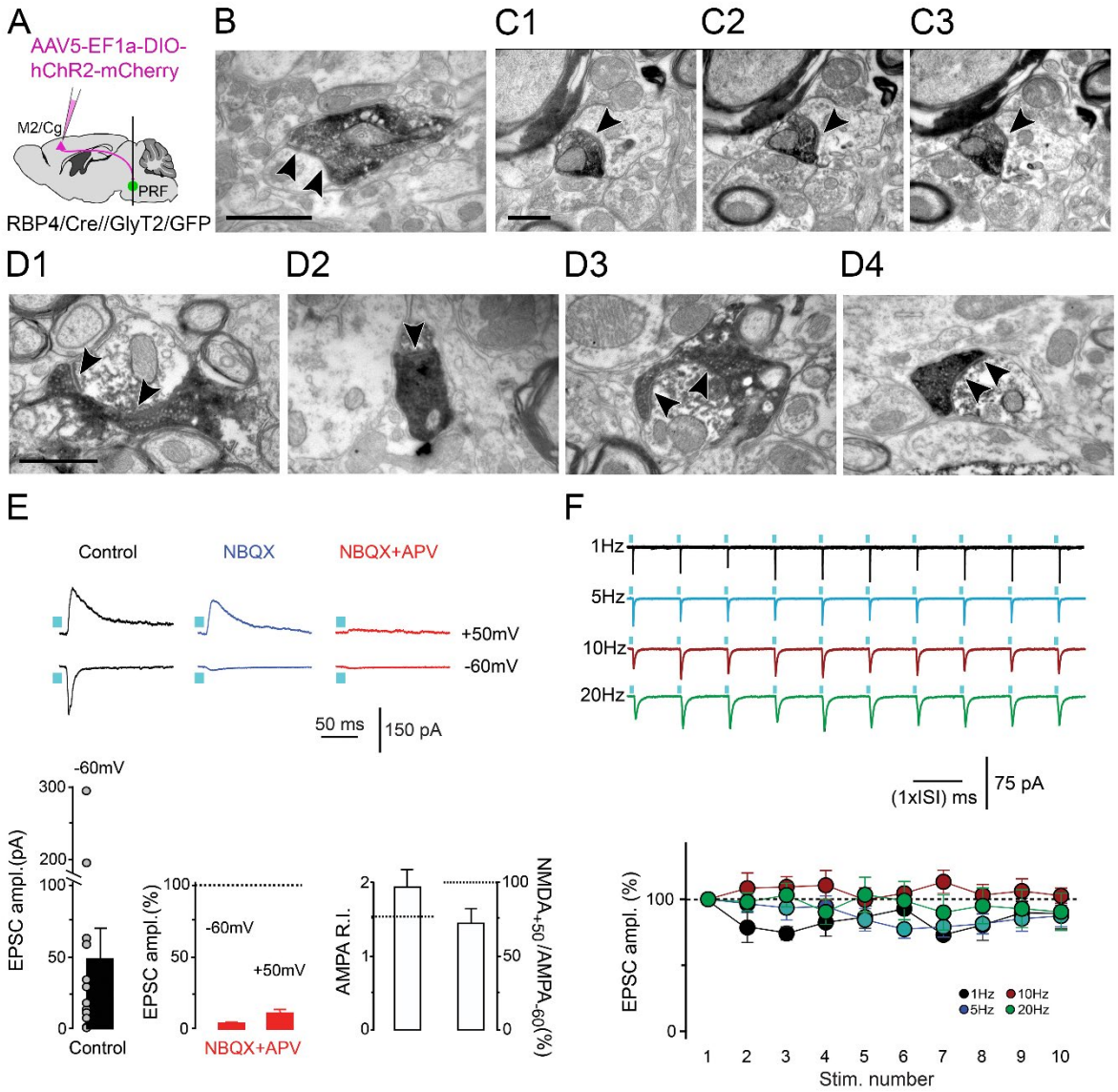

1242

1243 Figure 2. Cortical afferents target PRF/GlyT2+ cells and evoke a glutamatergic
1244 synaptic response.
1245 A) Scheme of anterograde tracing from the M2/Cg in the RBP4-Cre//GlyT2-eGFP
1246 mouse line.
1247 B-C) Electron micrographs of M2/Cg terminals (n=44, dark precipitates) in the PRF
1248 contacting mid-caliber dendrites.
1249 C1-C3) Serial EM images of the same axon terminal. Black arrowheads, synapses.
1250 D) Electron micrographs of M2/Cg terminals (DAB-Ni, dark, dense precipitate)
1251 establishing synapses on PRF/GlyT2+ dendrites (n=9, D1, D3, D4, DAB, light
1252 precipitate) and spines (n=1, D2).
1253 E) Optogenetically evoked (blue squares) AMPA and NMDA receptor-mediated
1254 components of the EPSCs elicited by M2/Cg terminals in the PRF. Traces from one
1255 exemplary experiment are shown above. Top: AMPA and NMDA components (n=16),
1256 control at -60 mV (n = 12; p = 0.002; Wilcoxon Signed-Rank Test) and +50 mV (n =
1257 12; p = 0.003; Wilcoxon Signed-Rank Test). Below, the graphs represent the results
1258 from all the experiments.
1259 F) Top: Light-evoked EPSC-s displayed no significant depression during stimulation
1260 trains, at all tested frequencies ranging from 5 to 20 Hz. Bottom: 89.1 ± 11.5 % (n = 6;
1261 p > 0.05; Wilcoxon Signed-Rank Test), 87.3 ± 8.2 % (n = 14; p = 0.03); Wilcoxon
1262 Signed-Rank Test), 102.7 ± 5.7 % (n = 10; p = 0.7; Wilcoxon Signed-Rank Test), 90.5
1263 ± 14.0 % (n = 12; p = 0.1; Wilcoxon Signed-Rank Test at 1 Hz, 5 Hz, 10 Hz and 20 Hz
1264 respectively.
1265 Source data are provided as a Source Data file. Data are represented as mean +/- SE.
1266 Scale bars: b) 1000 nm; c) 500 nm; d) 1000 nm.

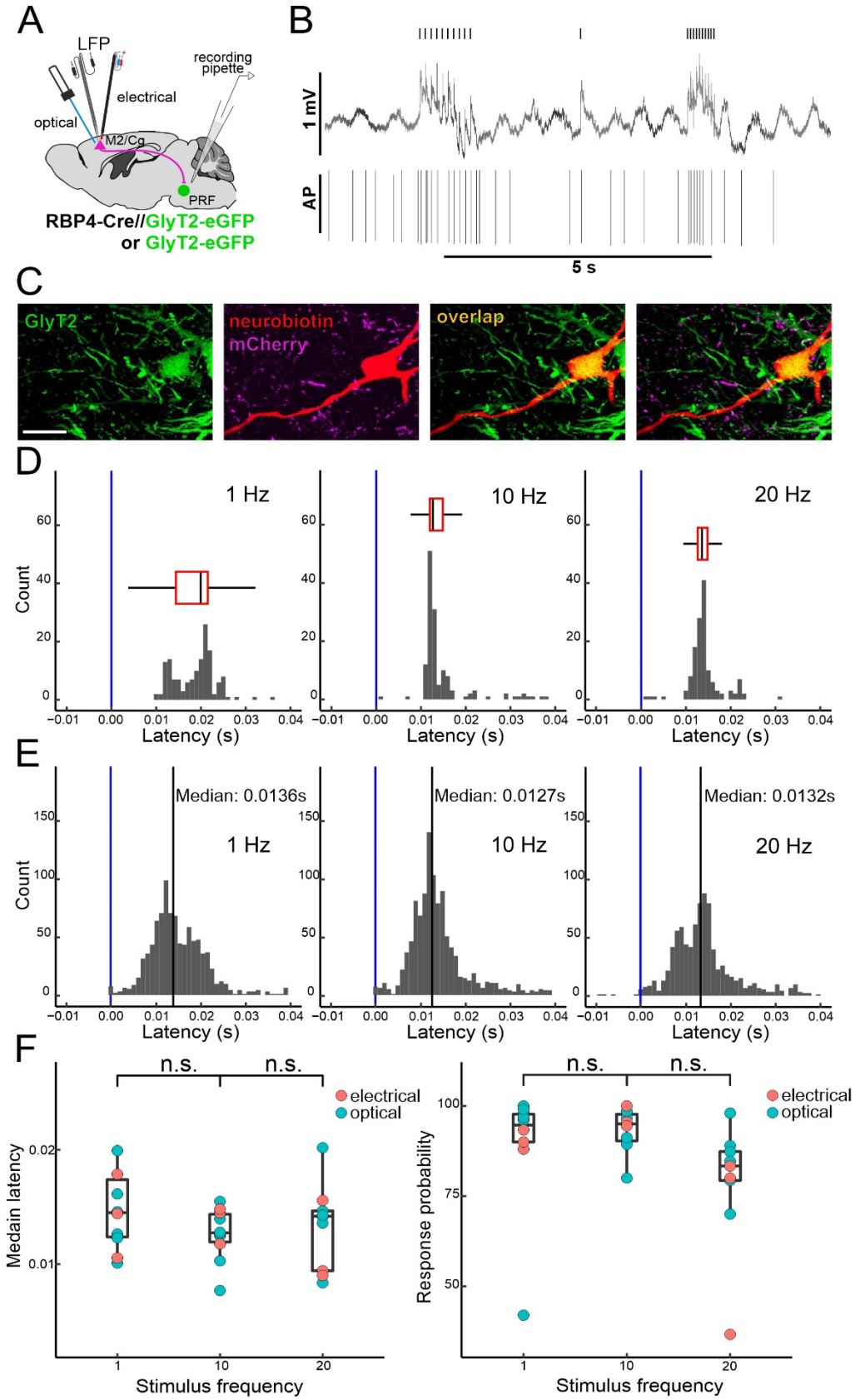
A
LFP
recording pipette
electrical
optical
M2/Cg
PRF
RBP4-Cre//GlyT2-eGFP
or GlyT2-eGFP
B
1 mV
AP
5 s
C
GlyT2
neurobiotin
mCherry
overlap
D
1 Hz
10 Hz
20 Hz
Count
Latency (s)
E
Median: 0.0136s
Median: 0.0127s
Median: 0.0132s
1 Hz
10 Hz
20 Hz
Count
Latency (s)
F
n.s.
n.s.
electrical
optical
Medain latency
Stimulus frequency
Response probability
Stimulus frequency

1267

1268 Figure 3. The effect of evoked cortical activity on PRF/GlyT2+ neurons

1269 A) Scheme of the experiments (n=10 mice: 7 mice with optogenetic 5-ms-long pulses
1270 at 1-20 mW (RBP4-Cre//GlyT2-eGFP), 3 mice with electrical 5 ms pulses at 1-2 mA
1271 (GlyT2-eGPF)).

1272 B) Representative stimulus-evoked cortical field activity and evoked firing of a
1273 glycinergic PRF neuron. Small ticks on the top indicate laser stimulation.

1274 C) Representative fluorescent micrograph of a recorded and labeled PRF/GlyT2+
1275 neuron. Green: GlyT2- eGFP; red: neurobiotin; magenta: M2/Cg fibers.

1276 D) Peristimulus time histograms (PSTH) of cortical stimulus-evoked firing in a
1277 representative PRF/GlyT2 neuron at 1, 10, and 20 Hz stimulation frequencies.
1278 Response probability and median latency are visualized by box plots.1 Hz: probability
1279 92.86%, 12.5 ms peak +/- SEM; 10 Hz: probability: 92.86%, 12.6 ms peak +/- SEM,
1280 20 Hz: probability 84.06%, 14.5 ms peak +/-SEM.

1281 E) Population PSTHs of juxtacellularly recorded and labeled PRF/GlyT2+ neurons
1282 (n=10) at 1, 10, and 20 Hz. 1 Hz median: 0.0136 s,10 Hz median: 0.0127 s, 20 Hz
1283 median: 0.0132 s.

1284 F) Median latency (left) 1 vs. 10 Hz, n.s. p=0.22; 10 Hz vs. 20 Hz n.s. p=0.3, Mood's
1285 median test and response probability (right) 1 vs. 10 Hz, n.s p=0.59; 10 Hz vs. 20 Hz
1286 n.s. p=0.65 Mood's median test of the PRF/GlyT2+ neurons.

1287 * 0.05<p; ** 0.01<p; *** p<0.001; n.s. - no significant difference. Source data are
1288 provided as a Source Data file

1289 Scale bars: c) 20 µm.

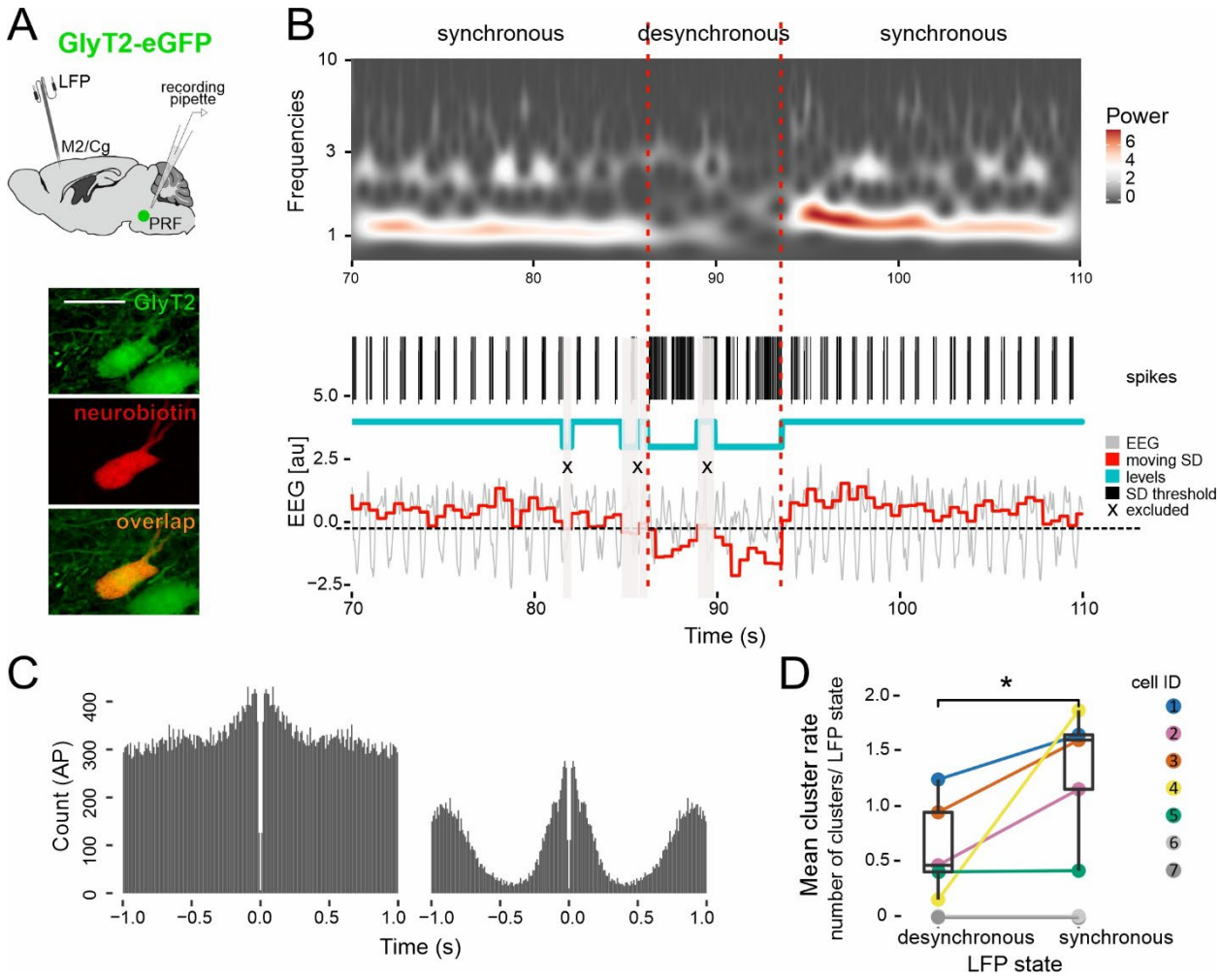

1290

1291 Figure 4. The effect of spontaneous cortical activity on PRF/GlyT2+ neurons

1292 A) Scheme of the experiments (n= 7 mice) and a posthoc identified PRF/GlyT2+ (n=7,

1293 green) neuron filled with neurobiotin (red) and the overlapping (yellow) (bottom)

1294 B) A representative example of a spontaneous state change under light ketamine-

1295 xylazine anesthesia together with the firing activity of a PRF/GlyT2+ cell.

1296 Top: Wavelet transformation of the cortical LFP activity. Middle: Action potentials of a

1297 PRF/GlyT2+ cell, thick black lines correspond to the first action potential of the

1298 detected clusters. Blue line: synchronized and desynchronized states. Bottom: The

1299 raw LFP signal is shown in grey, and the amplitude variance of the LFP signal (moving

1300 SD in a sliding window) is in red. The black dashed line represents the variance

1301 threshold for synchronized and desynchronized periods. Periods labeled with X (gray
1302 shading) are transient states, excluded from the analysis (see Methods).
1303 C) Autocorrelogram of a representative neuron during synchronized and
1304 desynchronized periods.
1305 D) Mean cluster rate (number of clusters/LFP state length) during synchronized
1306 (n=348, mean: 1.32, SD: 0.57, median: 1.59) and desynchronized periods (n=270).
1307 The two neurons shown in gray did not fire rhythmic AP clusters. (n=7, Wilcoxon
1308 Signed-Rank Test, p=0.032) * 0.05<p; ** 0.01<p; *** p<0.001; n.s. - no significant
1309 difference.
1310 Source data are provided as a Source Data file. Scale bars: A) 20 μm.

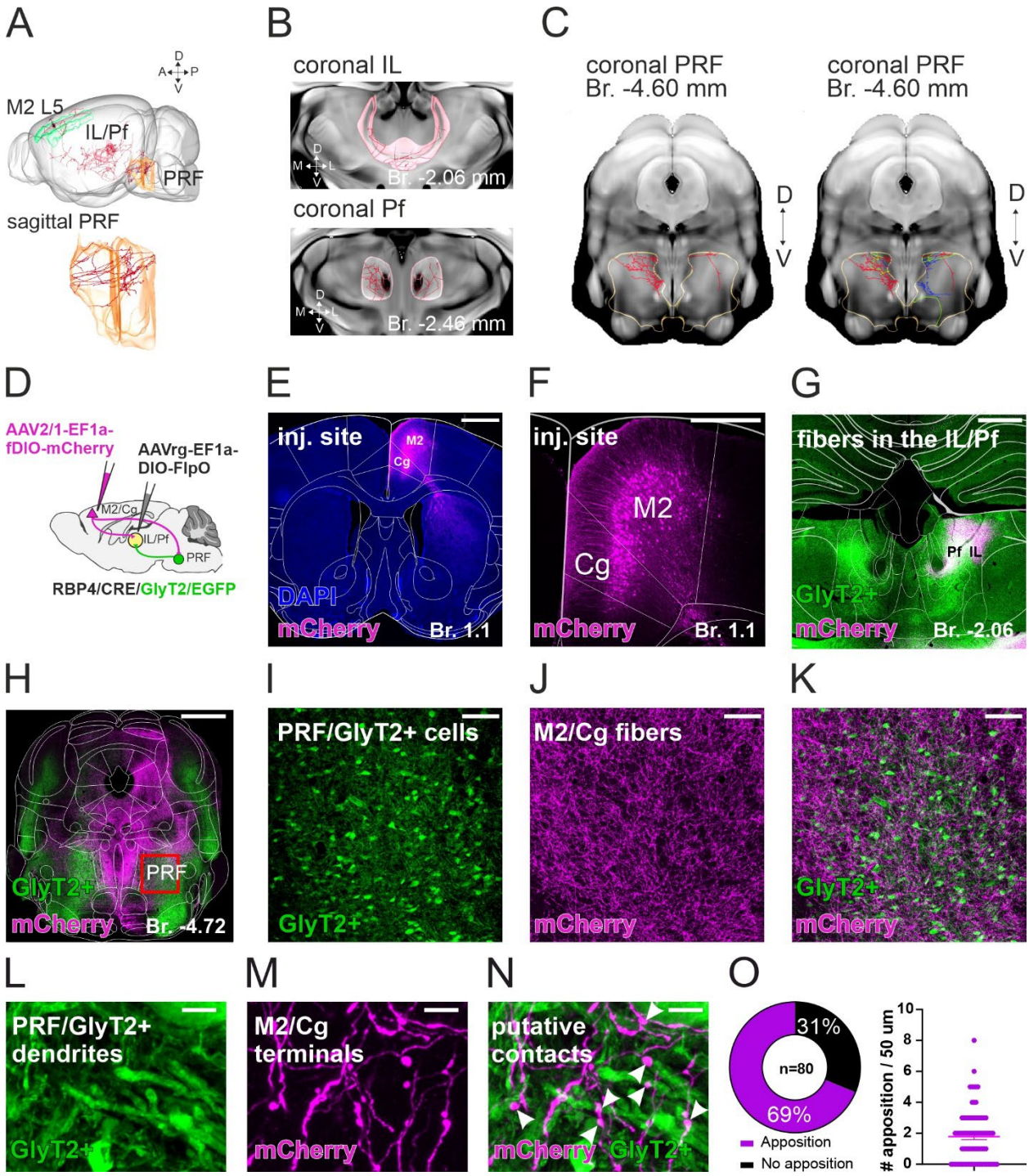

1311

1312 Figure 5. Co-innervation of PRF and thalamus by M2/Cg L5 neurons

1313 A) Reconstruction of a representative M2 L5 (AA0245) neuron from the Mouse Light

1314 Neuron Browser database which innervates both PRF and IL/Pf (top). Axon arbor of

1315 the representative M2 L5 neuron (AA0245) at the sagittal level in the PRF (bottom).

1316 B) Axon arbor of the representative M2 L5 neuron (AA0245) in the IL (top) and Pf
1317 (bottom)
1318 C) Axon arbor of the representative M2 L5 neuron (AA0245) (left in red) and of 4 L5
1319 neurons in the PRF (right, red, yellow, blue and green) that have 10 or more axonal
1320 end points in the PRF and also innervate IL/Pf with multiple endpoints.
1321 D) Scheme of the viral tracing to label PRF collaterals of thalamus-projecting M2/Cg
1322 cells.
1323 E) Low-power confocal micrograph of the cortical M2/Cg injection site.
1324 F) High-power confocal fluorescent image of the thalamus-projecting M2 L5 neurons.
1325 G) Merged confocal image of the labeled thalamus-projecting M2/Cg cortical fibers
1326 (magenta) and PRF/GlyT2+ fibers (green) in the thalamus.
1327 H) Merged, low power confocal image of the labeled thalamus-projecting M2/Cg
1328 cortical fibers (magenta) and PRF/GlyT2+ fibers (green) in the brainstem.
1329 I-K) Confocal micrographs of the PRF/GlyT2+ cells (green, I), anterogradely labeled
1330 thalamus-projecting M2/Cg cortical fibers (magenta, J), and their merged image (K).
1331 L-N) High power confocal microscopic image of close apposition between the
1332 PRF/GlyT2+ dendrites (green, L) and thalamus-projecting M2/Cg fibers (magenta, M).
1333 Arrows, putative contacts in (N).
1334 O) Percentage of innervated PRF/GlyT2+ dendrite (left) and the mean number of the
1335 close apposition per dendritic segment (right).
1336 Source data are provided as a Source Data file. Scale bars: E) 1 mm, F-G) 500 μm H)
1337 1mm I-K) 100 μm L-N) 5 μm.

1338

1339

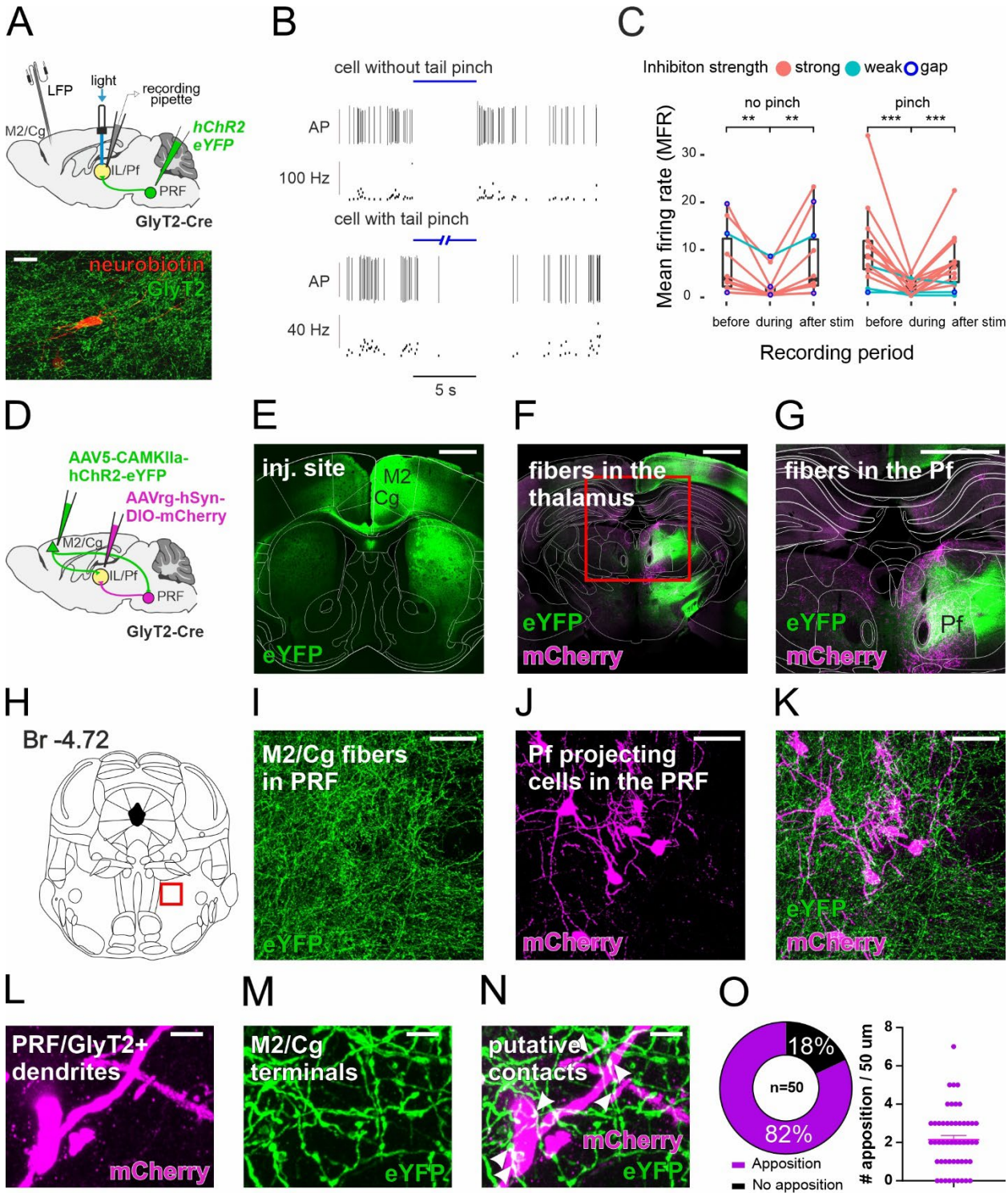

Figure 6. Inhibitory action and cortical innervation of thalamus-projecting PRF/GlyT2+ Cells

A) Top: Scheme of the juxtacellular recordings (n=13 mice, n=23 neurons). Bottom: Post hoc identified IL/Pf neuron surrounded by GlyT2+ fibers.

1345 B) Response of two representative IL/Pf thalamic neurons to optogenetic activation of
1346 PRF/GlyT2+ fibers (top, 5 sec stimulation, without a tail pinch, bottom, 30 sec
1347 stimulation with a tail pinch). Top: discriminated action potentials (AP), 5 sec
1348 stimulation, without tail pinch. Bottom: instantaneous firing rate (blue line = laser ON),
1349 30 sec stimulation with a tail pinch.
1350 C) Mean firing rate (MFR) of the recorded IL/Pf thalamic neurons before, during, and
1351 after the photoactivation PRF/GlyT2+ fibers. (33 Hz, 5 ms pulse width, laser power 10
1352 mW, 5-30 sec duration). Strongly inhibited, (red circles, n=19 cell), weakly inhibited
1353 (light blue circles, n=4, see Methods) and neurons responding with a post-stimulus
1354 gap (dark blue circle, n=4) are indicated. No pinch (left) and pinch (right) conditions
1355 are shown separately. No pinch MFR before vs. stim p=0.002; no pinch MFR stim vs
1356 after p=0.002 n=10 cells; pinch before vs. stim p=0.00012; pinch MFR stim vs. after
1357 p= 0.00085, n=14 cells; Wilcoxon Signed-Rank Test.
1358 D) Scheme of the double conditional viral tracing to label cortical inputs to thalamus
1359 projecting PRF/GlyT2+ cells.
1360 E) Low-power confocal micrograph of the cortical injection site.
1361 F-G) Merged confocal image of the M2/Cg cortical fibers (green) and PRF/GlyT2+
1362 fibers (magenta) in the thalamus. The red rectangle in F indicates the position of the
1363 G micrograph.
1364 H) Coronal, stereotactic image of the brainstem. The red rectangle indicates the
1365 position of the I-K micrographs.
1366 I-K) Confocal micrographs of the anterogradely labeled M2/Cg cortical fibers (green,
1367 I), retrogradely labeled thalamus-projecting PRF/GlyT2+ cells (magenta, J), and their
1368 merged image (K).

1369 L-N) High power confocal microscopic image of the thalamus-projecting PRF/GlyT2+
1370 dendrites (magenta, L) and M2/Cg fibers (magenta, M) and their putative contacts (N,
1371 arrowheads).
1372 O) Percentage of innervated thalamus-projecting PRF/GlyT2+ dendrite (left) and
1373 mean number of the close apposition per dendritic segment (right)
1374 * 0.05<p; ** 0.01<p; *** p<0.001; n.s. - no significant difference. Source data are
1375 provided as a Source Data file. Scale bars: A) 20 μm E-G) 1 mm I-K) 50 μm L-N) 5
1376 μm.
1377

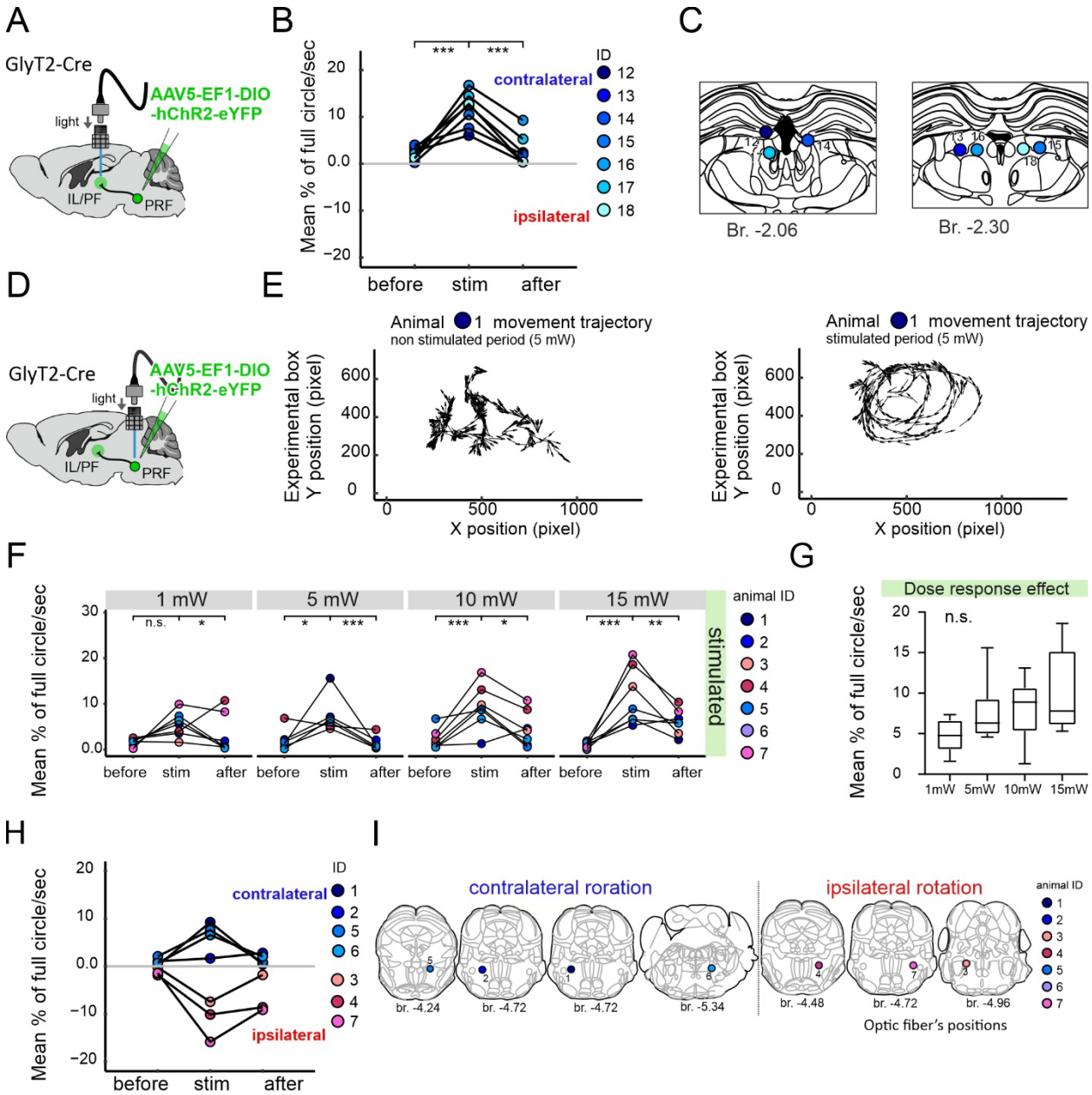

Figure 7. Rotational movements evoked by axonal vs somatic photoactivation of PRF/GlyT2+neurons

A) Experimental design of the photoactivation of thalamus-projecting PRF/GlyT2+ cells via their fibers in the thalamus (n=7 fiber optic fibers).

B) Contralateral rotations (n=7 fiber optics) displayed as mean rotation angle before, during, and after the stimulus periods following PRF/GlyT2+ fiber stimulation in Pf. The figure represents the average percentage of a full 360° circle per second.

1386 (χ^2=10.6, p=0.005, Friedman test following Durbin-Conover post-hoc, Before vs stim
1387 p<0.001; stim vs after p=<0.001)
1388 C) Schematic view of post hoc identified 7 optic fiber positions for experimental
1389 animals in Pf.
1390 D) Experimental design of the photoactivation of PRF/GlyT2+ somata in the PRF (n=7
1391 fiber optics).
1392 E) Movement trajectory in one representative mouse displaying contralateral turning
1393 (mouse ID: 1). Non-stimulated period (left), stimulated period (right) at 5 mW in the
1394 PRF.
1395 F) Comparison of the absolute values of the mean rotation angle before, during, and
1396 after the PRF stimulus periods in the 7 experimental mice (Friedman test following
1397 Durbin-Conover post-hoc; 1 mW χ^2=6, p=0.050; before vs. stim p=0.073; stim vs. after
1398 p=0,012; 5 mW χ^2=8.33, p=0.016; before vs. stim p=0.038; stim vs. after p<0.001; 10
1399 mW χ^2=10.3, p=0.006; before vs. stim p<0.001; stim vs. after p=0.014; 15 mW χ^2=12.3,
1400 p=0.002; before vs. stim p=<0.001; stim vs. after p=0.004 5 mW, χ^2=8.333, p=0.012;
1401 G) Lack of significant dose-response effect on rotation (Friedman test χ^2=7, p=0.072).
1402 H) Contralateral (n=4 animals, blueish shades) and ipsilateral (n=3 animals, reddish
1403 shades) rotations following PRF/GlyT2 somatic stimulations. The color code of the
1404 animals is the same as in F.
1405 I) Schematic view of post hoc identified optic fiber position (n=7) in PRF for the 7
1406 experimental mice. Right: fiber optic positions inducing contralateral rotation; left: fiber
1407 optic positions inducing ipsilateral rotation. Same notation as in G).
1408 * 0.05<p; ** 0.01<p; *** p<0.001; n.s. - no significant difference. Source data are
1409 provided as a Source Data file.

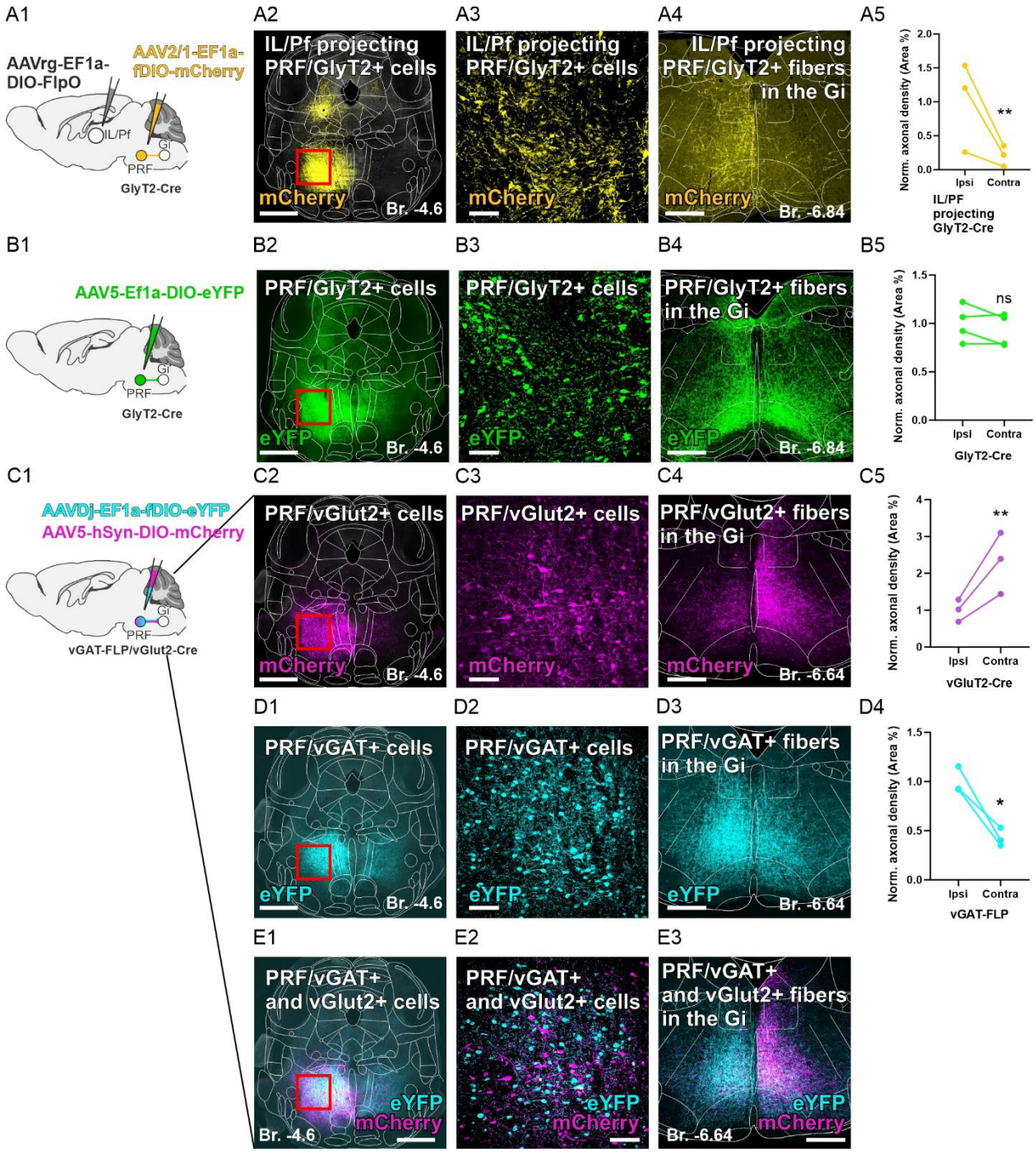

Figure 8. Selective ipsilateral innervation of the gigantocellular nucleus by thalamus projecting PRF/GlyT2+ cells

A1) Experimental design to label thalamus-projecting PRF/GlyT2 cells+ and their axons (n=3 mice).

1416 A2-3) Fluorescent micrograph about virus injection site in the PRF. The red rectangle
1417 on A2 indicates the position of the A3 micrograph.
1418 A4) Ipsilateral projection of the thalamus-projecting PRF/GlyT2+ cells in the Gi (yellow)
1419 A5) Quantification of ipsilateral and contralateral axonal projections of the thalamus-
1420 projecting PRF/GlyT2+ cells in the Gi in GlyT2-Cre Mice (paired t-test, $t_{(2)}$=22.07,
1421 p=0.002, n=3 mice).
1422 B1) Experimental design to label all PRF/GlyT2 cells+ PRF (n=4 mice).
1423 B2-3) Fluorescent micrograph about virus injection site in PRF. The red rectangle on
1424 B2 indicates the position of the B3 micrograph.
1425 B4) Bilateral projection of the PRF/GlyT2+ cells in the Gi (green).
1426 B5) Quantification of the ipsilateral vs. contralateral axonal projections from
1427 PRF/GlyT2+ cells within the Gi Region in GlyT2-Cre mice (paired t- test, $t_{(3)}$=1.462,
1428 p=0.24, n=4 mice).
1429 C1) Scheme of mixed viral injection into PRF in vGAT-Flp/vGlut2-Cre (n=3 mice).
1430 C2-3) Fluorescent micrograph about virus injection site in PRF. The red rectangle on
1431 C2 indicates the position of the C3 micrograph.
1432 C4) Bilateral projection with contralateral dominance of PRF/vGlut2+ cells in the Gi
1433 (magenta).
1434 C5) Quantification of ipsilateral and contralateral axonal projections from
1435 PRF/vGluT2+ cells within the Gi Region in vGluT2-Cre/vGAT-FLP mice (paired t- test,
1436 $t_{(2)}$=19.04, p=0.0027, n=3 mice).
1437 D1-2) Fluorescent micrograph about virus injection site in PRF. The red rectangle on
1438 D1 indicates the position of the D2 micrograph
1439 D3) Bilateral projection with ipsilateral dominance pf PRF/vGAT cells in the Gi (cyan)

1440 D4) Quantification of ipsilateral and contralateral axonal projections from PRF/vGAT2+
1441 cells within the Gi Region in vGluT2-Cre/vGAT-FLP mice (paired t- test, $t(2)=5.61$,
1442 $p=0.0303$, n=3 mice).
1443 E1-2) Fluorescent micrograph about virus injection site in PRF. The red rectangle on
1444 E1 indicates the position of the E2 micrograph.
1445 E3) Merged image of PRF/vGAT (cyan) and PRF/vGlut2+ (magenta) fibers in the Gi
1446 * $0.05<p$; ** $0.01<p$; *** $p<0.001$; n.s. - no significant difference. Source data are
1447 provided as a Source Data file.
1448 Scale bars: A2/B2/C2/D1/E1) 500 μm; A3/B3/C3/D2/E2) 100 μm A4/B4/C4/D3/E3)
1449 500 μm
1450

1451